

# On rapid binary mass transfer – I. Physical model

Wenbin Lu <sup>1,2,★</sup>, Jim Fuller <sup>3</sup>, Eliot Quataert <sup>2</sup> and Clément Bonnerot <sup>4</sup>

<sup>1</sup>Departments of Astronomy and Theoretical Astrophysics Center, UC Berkeley, Berkeley, CA 94720, USA

<sup>2</sup>Department of Astrophysical Sciences, Princeton University, Princeton, NJ 08544, USA

<sup>3</sup>TAPIR, Walter Burke Institute for Theoretical Physics, Mail Code 350-17, Caltech, Pasadena, CA 91125, USA

<sup>4</sup>Niels Bohr International Academy, Niels Bohr Institute, Blegdamsvej 17, DK-2100 Copenhagen Ø, Denmark

Accepted 2022 November 26. Received 2022 October 30; in original form 2022 March 30

## ABSTRACT

In some semidetached binary systems, the donor star may transfer mass to the companion at a very high rate. We propose that, at sufficiently high mass-transfer rates such that the accretion disc around the companion becomes geometrically thick (or advection-dominated) near the disc outer radius, a large fraction of the transferred mass may be lost through the outer Lagrangian (L2) point, as a result of the excessive energy generated by viscous heating that cannot be efficiently radiated away. A physical model is constructed where the L2 mass-loss fraction is given by the requirement that the remaining material in the disc has Bernoulli number equal to the L2 potential energy. Our model predicts significant L2 mass-loss at mass transfer rates exceeding a few  $10^{-4} M_{\odot} \text{ yr}^{-1}$ . An equatorial circumbinary outflow (CBO) is formed in these systems. Implications for the orbital evolution and the observational appearance of the system are discussed. In particular, (1) rapid angular momentum loss from the system tends to shrink the orbit, and hence may increase the formation rate of mergers and gravitational-wave sources; and (2) photons from the hot disc wind are reprocessed by the CBO into longer wavelength emission in the infrared bands, consistent with *Spitzer* observations of some ultra-luminous X-ray sources.

**Key words:** binaries: general – gravitational waves – stars: mass-loss.

## 1 INTRODUCTION

Binary mass transfer is one of the key aspects of stellar evolution and has been extensively studied in the past few decades (Paczynski 1971). Observational constraints on the physics involved in the process come from the large number of systems that are undergoing or about to undergo mass transfer, as well as many other objects that experienced mass transfer in the past. Perhaps, the least well-understood cases are the short-lived systems where the donor transfers mass to the companion at rates higher than about  $10^{-4} M_{\odot} \text{ yr}^{-1}$  and large uncertainties exist in predicting the fate of these systems (Podsiadlowski, Joss & Hsu 1992; Langer 2012; Ivanova et al. 2013; Postnov & Yungelson 2014).

Some physical examples potentially reaching such high-mass transfer rates are: (1) the Galactic micro-quasar SS433 (Fabrika 2004) and some extragalactic ultra-luminous X-ray sources (ULXes; Kaaret, Feng & Roberts 2017); (2) binaries where the donor transfers mass to the companion on the Kelvin–Helmholtz time-scale of its envelope, such as massive ( $\gtrsim 10 M_{\odot}$ ) Hertzsprung-gap stars undergoing envelope expansion in a binary with period less than  $10^3$  d (van den Heuvel, Portegies Zwart & de Mink 2017; Marchant et al. 2021; Klencki et al. 2021), and short-period (less than 2 d) helium star–neutron star (NS) binaries prior to the formation of merging double NSs (Tauris, Langer & Podsiadlowski 2015); (3) binaries undergoing unstable overflow just before the common envelope (CE) phase or stellar merger (Paczynski & Sienkiewicz 1972; Hjellming &

Webbink 1987; Soberman, Phinney & van den Heuvel 1997; Ge et al. 2010; Pavlovskii et al. 2017; Metzger et al. 2021), and (4) pre-supernova binaries where one of the stars may rapidly expand in the final stages of nuclear burning weeks to decades before the explosion (Quataert & Shiode 2012; McIey & Soker 2014; Fuller 2017; Wu & Fuller 2021). Gravitational wave sources detected in the past few years provide new constraints on the mass transfer physics by sampling the end products of some of these systems (e.g. Abbott et al. 2020, 2021).

The goal of this paper is to study the hydrodynamics of the transferred mass by modelling the super-Eddington accretion disc around the companion as well as the interaction between the material driven away from the disc and the binary Roche potential. We propose that, at mass-transfer rates exceeding a critical value (to be calculated in this work) such that the accretion disc around the companion becomes geometrically thick (or advection-dominated) near the disc outer radius, an order unity fraction of the transferred mass may be lost from the system through the outer Lagrangian (L2) point. This is because the advection-dominated accretion flow in the outer disc is energetically capable of driving material to L2 equipotential surface and beyond (Narayan & Yi 1994, 1995). We construct a physical model for the accretion disc and calculate the fraction of the transferred mass that is lost through the L2 point.

Binary mass transfer at such a high rate has been previously considered by King & Begelman (1999) and Begelman, King & Pringle (2006), who propose that the majority of the transferred mass is blown away to infinity in the form of a fast super-Eddington wind. However, because lifting material to the L2 potential is much less energetically demanding than to infinity, it is likely that the system

\* E-mail: [wenbinlu@berkeley.edu](mailto:wenbinlu@berkeley.edu)

takes the more energetically efficient solution, which is described in this paper. Evidence for such a solution has been seen in numerical simulations by Bisikalo et al. (1998), Sytov et al. (2007), MacLeod, Ostriker & Stone (2018a, b) for systems right before the onset of the CE phase, although these works did not treat the viscous accretion onto the companion. Another prescription used in binary population synthesis calculations is that when the mass-transfer exceeds a critical rate, the system undergoes CE evolution (Ivanova et al. 2003). Our model allows explicit calculation of the binary orbital evolution taking into account the angular momentum carried away by L2 mass-loss. This does not necessarily lead to CE. Only the cases with extremely rapid orbital shrinkage on a dynamical time may undergo CE evolution.

Observationally, the binary system SS433 in our Galaxy, with a mass-transfer rate of the order  $10^{-4} M_{\odot} \text{ yr}^{-1}$  (Fabrika 2004), indeed appears to be undergoing L2 mass-loss. Studies of the optical emission line profiles and spatially resolved radio/infrared images show the existence of equatorial circumbinary outflowing material (e.g. Filippenko et al. 1988; Paragi et al. 1999; Blundell et al. 2001; Blundell, Bowler & Schmidtobreick 2008; Waisberg et al. 2019). Many nearby ( $\lesssim 10$  Mpc) ULXes have optical and infrared (IR) counterparts (Tao et al. 2011; Gladstone et al. 2013; Heida et al. 2014). The spectral energy distributions (SEDs) of some of these sources show IR excess far above the power-law extrapolation from the optical bands (Heida et al. 2014; López et al. 2017; Lau et al. 2017, 2019), and these authors have suggested that the IR excess might be due to a red supergiant star (or supergiant Be star) donor or circumstellar dust. In our model, a system undergoing L2 mass-loss forms an equatorially concentrated circumbinary outflow (CBO), and we show that the observed IR excess is consistent with reprocessing of the disc wind emission by the CBO.

This paper is organized as follows. We present the model for the accretion disc at different mass-transfer rates and binary separations, and then determine the fate of the transferred mass in Section 2. Then in Section 3, the effect of L2 mass-loss on the binary orbital evolution is discussed. In Section 4, we calculate the radiative appearance of a system undergoing L2 mass-loss, focusing on the reprocessing of the disc wind emission by the circumbinary material. We discuss the limitations of our model in Section 5. A summary of our results is provided in Section 6. The logarithm of base 10 is denoted as log throughout the paper.

## 2 FATE OF THE OVERFLOWING MASS

In this section, we first review the standard Roche lobe geometry and define the parameters of the problem in Section 2.1. Then, we present the model for the accretion disc around the accretor including possible L2 mass-loss. Two different regimes of mass-transfer rates are discussed in Section 2.2 (high  $|\dot{M}_1|$ ) and Section 2.3 (low  $|\dot{M}_1|$ ).

### 2.1 Standard Roche lobe geometry

Let us consider a primary donor star of mass  $M_1$  with a given density profile and a point-mass companion of mass  $M_2$  in a circular orbit. The separation between the centres of the two stars is  $a$ . We define the mass ratio as

$$q = \frac{M_2}{M_1}, \text{ and set } \mu = \frac{q}{1+q}. \quad (1)$$

Under the assumption that both stars are in synchronous rotation at the Keplerian angular frequency and that nearly all the mass of the primary is concentrated near its centre, the Roche potential  $\Phi(\mathbf{r})$  is

given by

$$\frac{-a \Phi(\mathbf{r})}{G(M_1 + M_2)} = \frac{1-\mu}{|\mathbf{r}|} + \frac{\mu}{|\mathbf{r} - \hat{\mathbf{x}}|} + \frac{(x-\mu)^2 + y^2}{2}, \quad (2)$$

where we have placed the origin of the Cartesian coordinate system at the centre of the primary star, with  $\hat{\mathbf{x}}$  pointing towards the secondary and  $\hat{\mathbf{z}}$  towards the direction of the angular momentum vector, and the coordinates have been normalized by the orbital separation  $a$ . The position of the secondary is  $\mathbf{r}_2 = \hat{\mathbf{x}}$  and the center of mass of the binary system is located at  $\mathbf{r}_{\text{CM}} = \mu \hat{\mathbf{x}}$ . The positions of stationary points are the simultaneous solutions of  $\partial_x \Phi = \partial_y \Phi = \partial_z \Phi = 0$ . The three Lagrangian points along the  $\hat{\mathbf{x}}$  axis are obtained by solving the two equations above while setting  $y = z = 0$ , and this gives

$$(1-\mu) \frac{x}{|x|^3} + \mu \frac{x-1}{|x-1|^3} - x + \mu = 0. \quad (3)$$

The three solutions are denoted as  $x_{L1}, x_{L2}, x_{L3}$ , and the corresponding dimensionless potentials are denoted as  $\Phi_{L1}, \Phi_{L2}, \Phi_{L3}$ . We find the following quadratic polynomial fits to the numerical solutions

$$\begin{aligned} x_{L1} &\approx -0.0355(\log q)^2 - 0.251 \log q + 0.500, \\ x_{L2} &\approx 0.0756(\log q)^2 + 0.424 \log q + 1.699, \end{aligned} \quad (4)$$

which apply for  $0.01 < q < 1$  with fractional errors  $\lesssim 0.3$  per cent and are slightly more accurate than linear fits (e.g. Plavec & Kratochvil 1964; Frank, King & Raine 2002). By symmetry, the Lagrangian positions for  $q > 1$  are  $1 - x_{L1}(1/q)$  and  $1 - x_{L2}(1/q)$ .

The radius  $R_v$  of a volume-equivalent sphere for each equipotential surface (denoted by its dimensionless potential  $\Phi_p$ ) around the primary star can be obtained in the following way. The potential gradient on the equipotential surface far from the L1 nozzle is dominated by the gravity of the primary,  $d\Phi_p/dR_v \approx (1+q)^{-1} R_v^{-2}$ , and this can be combined with the boundary condition  $R_v(\Phi_{L1}) = R_{v,L1}$  to obtain

$$R_v(\Phi_p) \approx \frac{1}{R_{v,L1}^{-1} - (1+q)(\Phi_p - \Phi_{L1})}, \quad (5)$$

where the volume-equivalent radius of the Roche lobe is given by (Eggleton 1983)

$$R_{v,L1} \approx \frac{0.49}{0.6 + q^{2/3} \ln(1 + q^{-1/3})}. \quad (6)$$

A schematic picture of the model is shown in Fig. 1 for the case of  $q < 1$  (the donor being more massive). When the primary star overfills its Roche lobe, mass starts to overflow towards the secondary at a rate  $|\dot{M}_1|$  in the form of a super-sonic stream. We only consider the cases where the mass ratio is not extreme ( $q$  not much less or much greater than one), so  $R_v(\Phi_{L2})$  is larger than  $R_v(\Phi_{L1})$  by 10s of per cent. This means that, if the primary manages to expand beyond the  $\Phi_{L2}$  surface, the Roche lobe (or the  $\Phi_{L1}$  surface) is deeply inside the star where the density and pressure are very high, so the mass-transfer rate towards the secondary is much larger than that directly escaping from the L2 point (Pavlovskii et al. 2017; Marchant et al. 2021). Thus, in the following, we focus on the mass flow towards the secondary through the L1 nozzle (in between equipotential surfaces of  $\Phi_{L1}$  and  $\Phi_{L2}$ ), and our goal is to study the condition under which a significant fraction of the transferred mass through the L1 nozzle is lost beyond the L2 point.

In the case of  $q > 1$  (the accretor being more massive<sup>1</sup>), the L2 point is on the donor side and the L3 point is on the accretor

<sup>1</sup>Note that, in the case of  $q > 1$ , we still denote the donor as the primary star with mass  $M_1$  and the accretor as the secondary star with mass  $M_2$ .

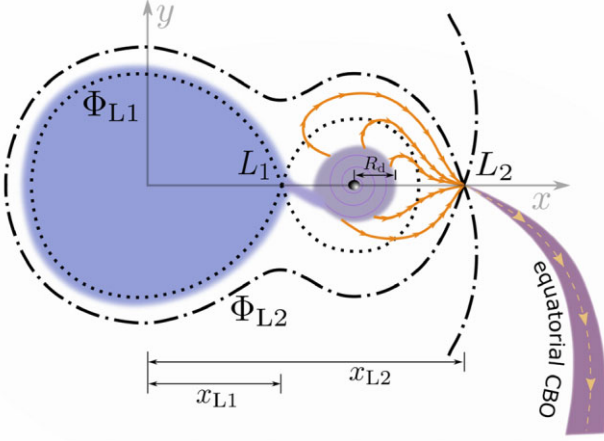


**Figure 1.** A broad-brush picture of the model. Two equipotential surfaces with potential energies  $\Phi_{L1}$  (dotted curve) and  $\Phi_{L2}$  (dashed-dotted curve) are shown in the corotating frame of the binary system. The primary star (left) fills up its Roche lobe and is transferring mass towards the secondary (right) through the L1 nozzle. When the mass-transfer rate exceeds a few  $10^{-4} M_{\odot} \text{ yr}^{-1}$ , a significant fraction of the transferred mass is lost through the L2 nozzle likely in the form of a supersonic stream. The stream from the L2 nozzle expands in width as it propagates to large distances from the binary system and forms an axisymmetric equatorially concentrated circumbinary outflow (CBO). The thick orange solid lines with arrows pointing from the accretion disc to the L2 point are only for schematic purpose, whereas our crude model does not provide an accurate description of the gas in this region.

side. In this work, we assume that the material can still be driven away from the accretion disc to reach the L2 point, but it must return to the donor side and fill the space in between the L1 and L2 equipotential surface. A potential concern is the counter-streaming motion above the donor's surface where the flow is subjected to the Kelvin–Helmholtz instability. Alternatively, the disc material with excessive energy (above  $\Phi_{L3}$ ) may leave the system from the nearby L3 nozzle. This alternative scenario of L3 mass-loss likely occurs for the nearly equal-mass case with  $q \approx 1$  and  $q > 1$  (see fig. 2 of Sytov et al. 2007). Nevertheless, even in the case of L3 mass-loss, the model presented in this paper should give qualitatively similar results, since the difference  $\Phi_{L3} - \Phi_{L2}$  is much smaller than the potential energy at the accretion disc radius  $|\Phi(R_d)|$  (defined in equation 9). For instance, when  $q = 2$ , we have  $\Phi_{L3} - \Phi_{L2} \approx 0.11 \Phi_0$ , whereas  $|\Phi(R_d)| \approx 2.48 \Phi_0$ , where  $\Phi_0 = G(M_1 + M_2)/a$ .

We do not consider the regime where the accretor is much more massive than the donor ( $q \gg 1$ ) because, in this limit, the L2 equipotential surface only has a very small lobe on the donor side. This means that the accretion disc and its outflow are nearly unaffected by the donor's gravity. It is possible that the majority of the mass driven away from the outer disc forms a quasi-spherical structure (similar to that found by Bobrick, Davies & Church 2017) instead of an equatorially concentrated CBO. Our model should be applicable for mass ratios from  $q \ll 1$  up to  $q \sim 3$ .

## 2.2 L2 mass-loss from the outer accretion disc

The supersonic stream leaving the L1 nozzle has specific angular momentum with respect to the secondary  $\ell \approx (1 - x_{L1})^2 a^2 \Omega$  (where  $\Omega = \sqrt{G(M_1 + M_2)/a^3}$ ). This is an approximation obtained under the assumption that the inertial-frame acceleration of the fluid elements in the stream is dominated by the secondary's gravity. This

angular momentum corresponds to a Keplerian circularization radius (Warner 1995)

$$R_c = \ell^2 / GM_2 \approx (1 - x_{L1})^4 a / \mu. \quad (7)$$

If the radius of the secondary is greater than  $R_c$ , then the transferred mass mostly lands on the accretor's surface. However, this only happens in the situation where the secondary is also close to filling its own Roche lobe (e.g. for mass transfer between two main-sequence stars or two white dwarfs of comparable masses).

In this paper, we restrict our analysis to the case where the secondary is smaller than the circularization radius,  $R_2 < R_c$  and an accretion disc forms. The outer edge of the disc viscously spreads to a slightly larger radius  $R_{d, \text{max}}$  where it is tidally truncated. The tidal truncation radius  $R_{d, \text{max}}$  is comparable to (about 80 per cent of) the volume-equivalent radius of the Roche lobe of the secondary (see Paczynski 1977; Hirose & Osaki 1990, for considerations based on orbit crossing), but the majority of the disc mass is at smaller radii closer to  $R_c$ . In the following, we consider a simplified one-zone model for the outer accretion disc at radius

$$R_d \simeq R_c. \quad (8)$$

The potential energy at radius  $R_d$  from the accretor can be obtained from equation (2), and when high-order terms  $\mathcal{O}(R_d^2/a^2)$  are ignored, the result can be simplified into

$$\begin{aligned} \Phi(R_d) &\approx -\frac{G(M_1 + M_2)}{a} \left[ 1 - \mu + \frac{\mu a}{R_d} + \frac{1}{2}(1 - \mu)^2 \right] \\ &= -\frac{GM_2}{R_d} \left[ 1 + \frac{(1 - \mu)(3 - \mu)}{2\mu} \frac{R_d}{a} \right]. \end{aligned} \quad (9)$$

The goal of this subsection is to understand the thermodynamic state and the fate of the disc material near  $R_d$ . In particular, we show that, when the mass-transfer rate is sufficiently high such that  $GM_2|\dot{M}_1|/R_d$  is comparable to the Eddington luminosity of the secondary, a large fraction of the transferred mass is lost through the L2 nozzle.

Because  $R_d$  is about 1/3 of the volume-equivalent radius of the secondary's Roche lobe (Warner 1995), the gravity on the disc gas is dominated by the secondary. The vertical pressure scale height  $H$  is given by the balance between pressure gradient and gravity in the direction perpendicular to the disc mid-plane

$$H = c_s / \Omega_K, \quad c_s = \sqrt{P/\rho}, \quad \Omega_K = \sqrt{GM_2/R_d^3}, \quad (10)$$

where  $\Omega_K$  is the Keplerian frequency,  $\rho$  is the density,  $c_s$  is the isothermal sound speed, and the total pressure  $P$  includes the contributions from gas  $P_g = \rho k_B T / \mu_g m_p$  ( $k_B, m_p$  being the Boltzmann constant and proton mass) and radiation pressure  $P_{\text{rad}} = a_r T^4 / 3$  ( $a_r$  being the radiation density constant). The gas pressure contains the mean molecular weight  $\mu_g$  which depends on the composition and ionization of the gas:  $\mu_g$  is 1.3/2.4  $\simeq$  0.54 for fully ionized solar abundance gas (with He-to-H number ratio of 0.1), 4/3 (or 2) for fully (or singly) ionized helium, and  $\gtrsim 2$  for heavier composition. In this work, we take  $\mu_g = 0.54$  as fiducial. The gas-radiation mixture is assumed to be in local thermodynamic equilibrium at the same temperature  $T$ , as a result of efficient coupling by absorption/emission as well as Compton scattering.

The dynamical evolution of the disc is driven by viscosity (Shakura & Sunyaev 1973),

$$\nu_{\text{vis}} = \alpha c_s H = \alpha H^2 \Omega_K, \quad (11)$$

and the corresponding viscous time is

$$t_{\text{vis}} = R_d^2 / \nu_{\text{vis}} = [\alpha (H/R_d)^2 \Omega_K]^{-1}, \quad (12)$$



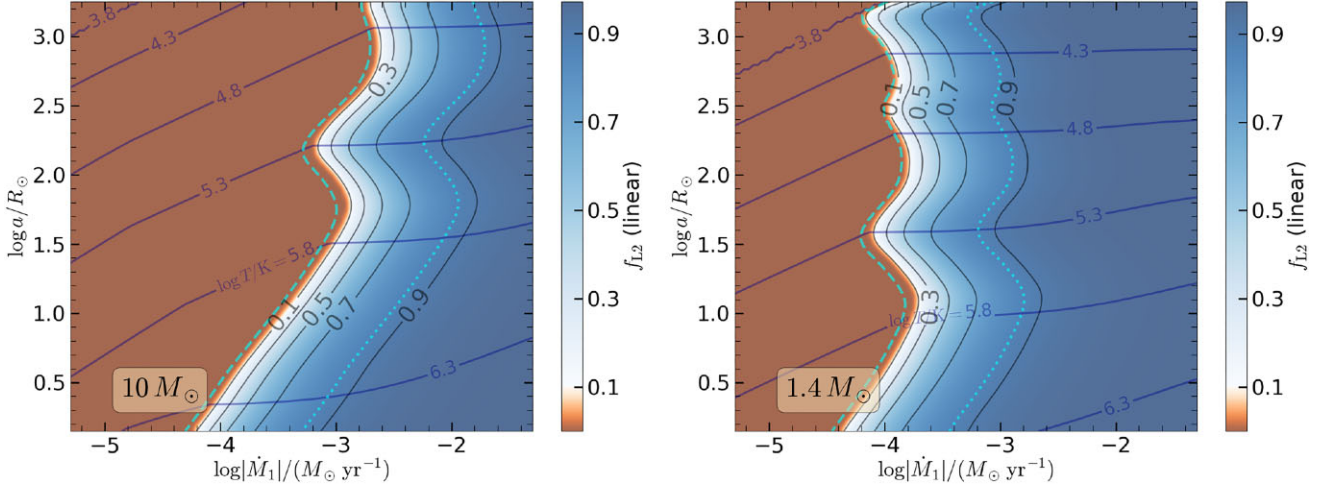


**Figure 2.** The outer disc solutions for a wide range of mass transfer rates  $|\dot{M}_1|$  and semimajor axis  $a$ . The dark blue contours show the disc temperature  $T$ , and the colour-shading and black contours show the L2 mass-loss fraction from the outer disc  $f_{L2}^{\text{outer}}$  (in linear scale). The left-hand panel is for secondary mass  $M_2 = 10 M_\odot$  (massive star or BH), and the right-hand panel is for  $M_2 = 1.4 M_\odot$  (NS). For both panels, we have fixed the mass ratio  $q = M_2/M_1 = 0.5$  and viscosity parameter  $\alpha = 0.1$ . The gas composition is H-rich at solar metallicity ( $X = 0.7$ ,  $Z = 0.02$ ). The cyan dashed and dotted lines in each panel indicate where  $(Q_{\text{adv}} + Q_{L2})/Q_{\text{rad}} = 0.1$  and 1, respectively (the latter roughly corresponds to where  $GM_2|\dot{M}_1|/R_d \simeq L_{\text{Edd},2}$ ). When the local viscous heating rate near  $R_d$  is comparable to the Eddington luminosity of the secondary, the disc becomes geometrically thick, and hence cooling due to the advective ( $Q_{\text{adv}}$ , equation 22) and L2-loss ( $Q_{L2}$ , equation 23) terms becomes important. We find that when the mass-transfer rate exceeds a threshold of about  $10^{-4} M_\odot \text{ yr}^{-1}$  (which is strongly modulated by the opacity variations), a significant fraction of the transferred mass is lost through the L2 nozzle.

where we will take a fiducial  $\alpha = 0.1$ . In a quasi-steady state, the dynamical evolution of the disc is controlled by continuous mass supply from the L1 nozzle, viscous accretion towards the secondary star, and possible mass-loss from the L2 nozzle. It may be tempting to include another mass-loss term from a fast wind that directly escapes the system (e.g. Piran 1977; King & Begelman 1999). This requires acceleration of gas near  $R_d$  to above local escape speed. This is much more energetically demanding than lifting the material to the L2 potential, and we assume that the gas takes the more energetically efficient path.

Note that viscous accretion drives a fraction of gas to much smaller radii  $R \ll R_d$ , where the Keplerian rotation velocity is much higher than the corotation speed at the L2 point, so the majority of the inner disc outflow launched from  $R \ll R_d$  is not strongly affected by the binary orbit and should escape the system as fast wind (Blandford & Begelman 1999). However, there could still be a small fraction of the outflow launched from the inner disc ( $R \ll R_d$ ) that is captured by the binary orbit and contributes to L2 mass-loss. This will be discussed later in the next subsection. For the moment, we focus on the gas near radius  $R_d$ .

We assume that a fraction  $f_{L2}$  of the mass inflow rate  $|\dot{M}_1|$  is channeled through the L2 nozzle, and the accretion rate is given by

$$(1 - f_{L2})|\dot{M}_1| \simeq \frac{M_d}{t_{\text{vis}}}, \quad M_d \simeq 2\pi\rho R_d^2 H, \quad (13)$$

where  $M_d$  is the disc mass and the parameter  $f_{L2}$  will be determined later in a self-consistent way. Let us define a dimensionless scale height

$$\theta \equiv H/R_d, \quad (14)$$

and hence the disc density is given by

$$\rho = \frac{(1 - f_{L2})|\dot{M}_1|}{2\pi\alpha\Omega_K R_d^3} \frac{1}{\theta^3}. \quad (15)$$

Then, equations (10–13) can be combined to give a relation between  $\theta$ , the disc temperature  $T$ , and the L2 mass-loss fraction  $f_{L2}$ ,

$$\frac{c_1 T^4}{1 - f_{L2}} \theta^3 - \theta^2 + c_2 T = 0, \quad (16)$$

where

$$c_1 = \frac{2\pi a_\tau \alpha R_d}{3\Omega_K |\dot{M}_1|}, \quad c_2 = \frac{k_B R_d}{GM_2 \mu_g m_p}. \quad (17)$$

On the other hand, the disc temperature is determined by energy conservation

$$Q_{\text{vis}}^+ + Q_{\text{sh}}^+ = Q_{\text{rad}}^- + Q_{\text{adv}}^- + Q_{L2}^-, \quad (18)$$

where the heating ( $Q^+$ ) and cooling ( $Q^-$ ) rates are defined below. We assume the disc to be rotating at the Keplerian frequency  $\Omega_K$ . The deviation from Keplerian rotation due to radial pressure gradient is small,  $\mathcal{O}(H^2/R_d^2)$ , and does not qualitatively affect our results. The viscous heating rate per unit mass is

$$\frac{Q_{\text{vis}}^+}{M_d} \simeq \frac{9}{4} \nu_{\text{vis}} \Omega_K^2 = \frac{9}{4} \frac{GM_2/R_d}{t_{\text{vis}}}. \quad (19)$$

The incoming stream strikes the disc near the outer edge and eventually circularizes to near-Keplerian motion close to  $R_d$ , and this generates a total shock heating rate of

$$Q_{\text{sh}}^+ \simeq |\dot{M}_1| \left( \Phi_{L1} - \Phi(R_d) - \frac{GM_2}{2R_d} \right), \quad (20)$$

where we have included the kinetic energy  $GM_2/2R_d$  but ignored the (subdominant) thermal energy of the circularized gas. The radiative cooling rate is given by

$$Q_{\text{rad}}^- \simeq 2\pi R_d^2 \frac{U_{\text{rad}} c}{\tau/2}, \quad \tau = \rho \kappa H, \quad (21)$$

where  $U_{\text{rad}} = a_\tau T^4$  is the radiation energy density,  $c$  is the speed of light,  $\tau$  is the optical depth in the vertical direction, and  $\kappa$  is the Rosseland-mean opacity. We have taken the vertical diffusive

radiative flux to be  $U_{\text{rad}}c/(\tau/2)$ , where the factor of 1/2 in the denominator is based on the consideration that most photons are generated at some height ( $\sim H/2$ ) away from the disc mid-plane where the optical depth is reduced compared to that of the entire disc. Note that we are interested in the regime where the disc is highly optically thick  $\tau \gg 1$  and we have checked that all our solutions satisfy this condition.

As for the opacity  $\kappa(\rho, T)$ , we smoothly blend the high-temperature ( $T \gtrsim 10^4$  K) tables from OPAL (Iglesias & Rogers 1996) and low-temperature ( $10^3 \lesssim T \lesssim 10^4$  K) tables by Ferguson et al. (2005), which include effects of molecules and dust grains. These tables are conveniently collected by the MESA code (Paxton et al. 2019) in the `/mesa/kap/` directory. Our fiducial gas composition is H-rich with mass fractions  $X = 0.7$  (H),  $Y = 0.28$  (He),  $Z = 0.02$  (metals, with solar abundance), for which the names of the opacity tables are ‘gn93\_z0.02\_x0.7.data’ and ‘lowT\_fa05\_gn93\_z0.02\_x0.7.data’. In the Appendix, we also show the results for H-poor gas composition with ( $X = 0$ ,  $Z = 0.02$ ) and for a low-metallicity case ( $X = 0.7$ ,  $Z = 0.001$ ). A key difference between using realistic opacity tables and analytic Kramer’s opacity is that the opacity is strongly enhanced near  $T \sim 2 \times 10^5$  K due to bound-bound transitions of Fe (Badnell et al. 2005), and the iron opacity bump increases the L2 mass-loss fraction.

The cooling rate per unit mass due to heat advection by the radial inflow is given by

$$\frac{Q_{\text{adv}}^-}{M_d} = v_r T \frac{ds}{dR} \simeq \frac{3}{2} \frac{U}{P} \frac{GM_2/R_d}{t_{\text{vis}}} \theta^2, \quad (22)$$

where  $s$  is the specific entropy and  $v_r \simeq -3v_{\text{vis}}/(2R_d)$  is the radial velocity driven by viscous angular momentum transfer. To obtain the second expression in equation (22), we have made use of  $Tds = dh - dP/\rho$ ,  $dh/dR \simeq h/R_d$  for the specific enthalpy  $h = (U + P)/\rho$  and total energy density  $U \simeq 3\rho k_B T/2\mu_g m_p + a_r T^4$ , and  $dP/dR \simeq P/R_d$ . Determining the precise radial gradients requires at least one-dimensional modelling for the entire disc (e.g. Blandford & Begelman 1999, 2004), and our qualitative results are only weakly affected by these numerical factors of order unity. Note that  $Q_{\text{adv}}^- \propto (H/R_d)^2$  means that advective cooling is only important for a geometrically thick disc.

Finally, we argue that mass-loss from the L2 nozzle occurs at sufficiently high mass-transfer rates. This is because, in the absence of L2 mass-loss (setting  $f_{L2} = 0$  in equations 13 and 18), if the disc is in the advection-dominated state ( $Q_{\text{adv}}^- \gg Q_{\text{rad}}^-$ ), the system necessarily leads to a positive Bernoulli number, as showed by Narayan & Yi (1994, 1995) and Blandford & Begelman (1999). The physical consequence is that a significant fraction of the transferred mass can be driven away from the system. The most energetically efficient way of achieving this is to push some gas slightly over the L2 nozzle, and this is subsequently accelerated by the torque from the binary and flies to very large distances (Shu, Lubow & Anderson 1979). Recent numerical simulations of binary mass transfer with adiabatic hydrodynamics (MacLeod et al. 2018b, a) indeed find L2 mass-loss and hence support our proposal, but future radiation magnetohydrodynamic (MHD) simulations are needed to further test our model.

Based on the above arguments, we take the cooling rate due to L2 mass-loss to be

$$Q_{L2}^- \simeq f_{L2} |\dot{M}_1| \left( \Phi_{L2} - \Phi(R_d) - \frac{GM_2}{2R_d} \right). \quad (23)$$

More realistically, when reaching the L2 point, the escaping gas may have specific energy higher than  $\Phi_{L2}$ , and the residual kinetic

energy and enthalpy will affect their kinematics at larger radii  $R \gg a$  (Pejcha, Metzger & Tomida 2016b). However, determining the residual energy of the escaping gas at the L2 point is beyond the scope of the current work as it requires detailed numerical simulations.

With the above heating and cooling rates, the energy conservation equation (18) can be written in the following dimensionless form

$$\begin{aligned} \frac{9}{4} - \frac{3U}{2P} \theta^2 + \frac{\Phi_{L1} - f_{L2} \Phi_{L2}}{(1 - f_{L2}) GM_2/R_d} \\ = \frac{\Phi(R_d)}{GM_2/R_d} + \frac{1}{2} + \frac{c_3 T^4}{(1 - f_{L2})^2 \kappa} \theta^2, \end{aligned} \quad (24)$$

where

$$c_3 = \frac{8\pi^2 a_r \alpha c R_d^2}{|\dot{M}_1|^2 \Omega_K}. \quad (25)$$

This equation has many interesting features. When  $f_{L2} = 0$  and ignoring the shock heating terms, we have recovered the thermodynamic equilibrium of a simple viscously accreting disc (e.g. Yuan & Narayan 2014). At very high accretion rates, the diffusion time becomes longer than the viscous time such that the disc is very thick  $\theta \sim 1$  (shock heating also slightly increases the thickness). When L2 mass-loss is significant ( $f_{L2} \sim 1$ ), it efficiently cools the disc to a thinner one. Note that in the extreme limit  $1 - f_{L2} \ll 1$ , the disc might become optically thin, and then the radiative diffusion term on the right hand side needs to be multiplied by a factor of  $(1 + 1/\tau)^{-1}$ , which gets rid of the diverging behaviour of  $(1 - f_{L2})^{-2}$ . We have checked that our solutions have  $\tau \gg 1$  throughout the parameter space, so this correction factor is not needed.

Now, we have two equations (16) and (24) for three unknowns:  $\theta$ ,  $T$ , and  $f_{L2}$ . To close the system of equations, we must introduce a model for  $f_{L2}$ , the fraction of the transferred mass that is lost through the L2 nozzle. We take the minimum  $f_{L2}$  such that the remaining gas in the disc is not able to reach the L2 potential surface. This solution is a stable equilibrium for the following reason. A larger  $f_{L2}$  than the minimum value cools the disc even more such that there would be a gap between the energy of the mass lost through L2 nozzle and the remaining disc material. This is not the most energetically efficient solution and is disfavoured by our physical intuition. On the other hand, a smaller  $f_{L2}$  than the minimum means that the remaining disc material still has enough energy to climb up the potential to the L2 point (provided that radiative cooling can be ignored). This would lead to more mass-loss through L2.

In realistic systems, there is likely a transient phase where  $f_{L2}$  can be either higher or lower than its minimum value, and subsequently, the system will evolve towards the equilibrium when causal contact between the edge of the disc and the L2 point is established. The equilibrium  $f_{L2}$  is calculated as follows.

In the adiabatic limit, the Bernoulli number of the disc material at radius  $R_d$  is given by

$$\text{Be}(R_d) = \frac{GM_2/R_d}{2} + \Phi(R_d) + h, \quad (26)$$

where the specific enthalpy is given by

$$h = \frac{U + P}{\rho} = \frac{5k_B T}{2\mu_g m_p} + \frac{4a_r T^4}{3\rho}. \quad (27)$$

The Bernoulli number describes the total (kinetic plus potential) energy content of the gas and stays constant along a given stream line in a non-viscous and non-turbulent system. It is likely that the shear motion for the gas flows at radii larger than  $R_d$  do not have enough time to develop strong (MHD) turbulence to affect the bulk motion. Thus, disc gas with  $\text{Be}(R_d) \gtrsim \Phi_{L2}$  is able to reach the L2

potential and hence escapes to much larger radii, if we ignore the radiative cooling along the way.

To capture the detailed dynamics of the gas escaping from the disc through the L2 nozzle, one has to carry out radiation-MHD simulations in three dimensions. This is left to be explored in future work. For an analytical estimate, we adopt the following prescription

$$\begin{cases} f_{L2} = 0, & \text{if } \text{Be}(f_{L2} = 0) < \Phi_{L2}, \\ \text{Be}(f_{L2}) = \Phi_{L2}, & \text{otherwise,} \end{cases} \quad (28)$$

This limits the Bernoulli number to less than  $\Phi_{L2}$  (see Margalit & Metzger 2016, for a similar treatment but in a different context). The maximum disc thickness  $\theta_{\max} R_d$  is given by  $\text{Be}(f_{L2}) = \Phi_{L2}$ ,

$$\frac{4c_1 T^4}{1 - f_{L2}} \theta_{\max}^3 + \frac{5}{2} c_2 T = \frac{\Phi_{L2} - \Phi(R_d)}{GM_2/R_d} - \frac{1}{2}, \quad (29)$$

where  $c_1$  and  $c_2$  have been defined in equation (17). The above equation can be combined with equation (16) to yield

$$\theta_{\max}^2 = \frac{3c_2 T}{8} + \frac{1}{4} \frac{\Phi_{L2} - \Phi(R_d)}{GM_2/R_d} - \frac{1}{8}. \quad (30)$$

If the solution under no L2 mass-loss,  $\theta(f_{L2} = 0)$ , exceeds this maximum thickness  $\theta_{\max}$ , then, we require some finite  $0 < f_{L2} < 1$  so as to maintain  $\theta(f_{L2}) = \theta_{\max}$ .

The above model allows us to solve for the L2 mass-loss fraction  $f_{L2}$  as a function of the mass-transfer rate  $\dot{M}_1$  and semimajor axis  $a$ . In the following, we denote the L2 mass-loss fraction from the outer disc near  $R_d$  as  $f_{L2}^{\text{outer}}$ , so as to differentiate it from the potential L2 mass-loss from the inner disc (see Section 2.3). The results from our model, for the accretion disc near radius  $R_d$ , are shown in Fig. 2, for two different secondary masses  $M_2 = 10 M_\odot$  (massive star or BH) and  $1.4 M_\odot$  (NS). We find that, when the mass-transfer rate exceeds a few times  $10^{-4} M_\odot \text{ yr}^{-1}$  such that the local viscous heating rate near  $R_d$  becomes comparable to the Eddington luminosity of the secondary  $L_{\text{Edd}, 2} = 4\pi GM_2 c / \kappa$  (where  $\kappa$  is the gas opacity at  $R_d$ ), an order-unity fraction of the transferred mass is directly lost from the outer disc through the L2 nozzle.

### 2.3 L2 mass-loss from the inner accretion disc

In this section, we consider lower mass-transfer rates at which the outer disc is not capable of driving L2 mass-loss because the gas is radiating efficiently. At lower mass-transfer rates for which  $f_{L2}^{\text{outer}} \approx 0$ , the inner disc can still launch an outflow near the spherization radius  $R_{\text{sph}} \ll R_d$  where  $GM_2 |\dot{M}_1| / R_{\text{sph}}$  is close to the Eddington luminosity of the secondary  $L_{\text{Edd}, 2}$  and hence the disc becomes geometrically thick (Shakura & Sunyaev 1973; Begelman 1978), provided that the secondary object is sufficiently small  $R_2 < R_{\text{sph}}$ . The spherization radius is given by

$$R_{\text{sph}} = \min \left[ R_d, \frac{(1 - f_{L2}^{\text{outer}}) |\dot{M}_1| \kappa}{4\pi c} \right]. \quad (31)$$

At small radii  $R_{\text{sph}} \ll R_d$  from the secondary, most of the disc material cannot find a (fine-tuned) stream line that directly connects to the L2 nozzle, so the natural way to remove the excessive energy from the system is to launch a wind<sup>2</sup> with asymptotic speed of the order  $\sqrt{GM_2/R_{\text{sph}}}$  (Blandford & Begelman 1999). Therefore, the energy

distribution of the gas near  $R_{\text{sph}}$  is in between  $-GM_2/2R_{\text{sph}}$  (most bound) and  $+GM_2/2R_{\text{sph}}$  (most unbound). Most of the unbound gas is not affected by the binary orbit and quickly escapes the system as a fast wind. However, a small fraction of the gas with energy of the order  $|\Phi_{L2}|$  can be captured by the binary potential and then flows out of the system through the L2 nozzle.

Based on the above argument, we propose the L2 mass-loss fraction from the inner disc to be

$$f_{L2}^{\text{inner}} \simeq (1 - f_{L2}^{\text{outer}}) \frac{|\Phi_{L2}|}{GM_2/R_{\text{sph}}}, \quad (32)$$

which is based on the assumption that the energy distribution near  $R_{\text{sph}}$  is flat between  $\pm GM_2/2R_{\text{sph}}$ . Since  $|\Phi_{L2}| \sim 0.1 GM_2/R_d$ , we see that  $f_{L2}^{\text{inner}}$  is of the order  $0.1 R_{\text{sph}}/R_d$  based on our prescription in equation (32).

Note that here  $L_{\text{Edd}, 2}$  is based on the gas opacity near  $R_{\text{sph}}$  and this is generally different from that near  $R_d$ . The gas temperature and density near  $R_{\text{sph}}$  can be estimated (for disc thickness  $\theta \simeq 1$ ) by

$$a_r T^4 + \frac{3\rho k_B T}{2\mu_g m_p} \simeq \frac{GM_2 \rho}{R_{\text{sph}}}, \quad \rho \simeq \frac{(1 - f_{L2}^{\text{outer}}) |\dot{M}_1|}{2\pi \alpha \Omega_K(R_{\text{sph}}) R_{\text{sph}}^3}. \quad (33)$$

We note that, for outflows to be launched from the inner disc, the secondary object must be sufficiently small  $R_2 < R_{\text{sph}}$ . Otherwise  $f_{L2}^{\text{inner}} = 0$ , and in this case, the secondary gains mass at a rate  $(1 - f_{L2}^{\text{outer}}) |\dot{M}_1|$  until it reaches near the break-up rotation rate.

Finally, we combine the L2 mass-loss from the outer and inner disc to obtain the *total* L2 mass-loss fraction

$$f_{L2} = f_{L2}^{\text{outer}} + f_{L2}^{\text{inner}}. \quad (34)$$

This is shown in Fig. 3, for two different secondary masses  $M_2 = 10$  and  $1.4 M_\odot$ , under the assumption that the secondary is a compact object with  $R_2 \ll R_{\text{sph}}$  (a BH or NS).

We find that the contribution to L2 mass-loss from the inner disc is small:  $f_{L2}^{\text{inner}}$  is at most a few percent in the parameter space where  $f_{L2}^{\text{outer}}$  is negligible. The overall trend is that, at a fixed binary separation, the total L2 mass-loss fraction increases linearly (since  $R_{\text{sph}} \propto |\dot{M}_1|$ ) with the mass-transfer rate until the viscous heating rate in the outer disc becomes comparable to  $L_{\text{Edd}, 2}$  and, beyond this mass-transfer rate, nearly all the transferred mass is lost through the L2 nozzle. The orbital evolution of the system is only strongly affected by the angular momentum loss associated with L2 mass-loss when  $f_{L2}$  becomes close to order unity (at which point  $f_{L2} \approx f_{L2}^{\text{outer}}$ ), so it is appropriate to ignore the effects of a small  $f_{L2}^{\text{inner}}$  on the orbital evolution.

### 3 BINARY ORBITAL EVOLUTION AND ACCRETION ONTO THE SECONDARY

In this section, we consider the effects of L2 mass-loss as well as accretion onto the secondary on the binary orbital evolution. The key result is that the angular momentum loss associated with the CBO

<sup>2</sup>There was a historic debate whether advection-dominated accretion flows (ADAFs) lose a substantial fraction of mass in unbound outflows (Narayan & Yi 1994, 1995; Narayan, Kato & Honma 1997; Blandford & Begelman 1999, 2004) or nearly all the material stays bound (Stone, Pringle & Begelman 1999; Abramowicz, Lasota & Igumenshchev 2000; Narayan, Igumenshchev &

Abramowicz 2000; Quataert & Gruzinov 2000; Igumenshchev, Narayan & Abramowicz 2003). Recent large-scale long-duration numerical simulations of adiabatic accretion flows (Narayan et al. 2012; Yuan, Wu & Bu 2012) show that unbound outflows are generated in the regions beyond tens of gravitational radii ( $R_g = GM_2/c^2$ ) from a black hole accretor, provided that the simulation reaches inflow equilibrium up to about  $100 R_g$ . In our current case, since photons are largely trapped by the accretion flow at small radii from the accretor  $R < R_{\text{sph}}$ , this region of the disc is similar to ADAFs that are radiatively inefficient at very low accretion rates.



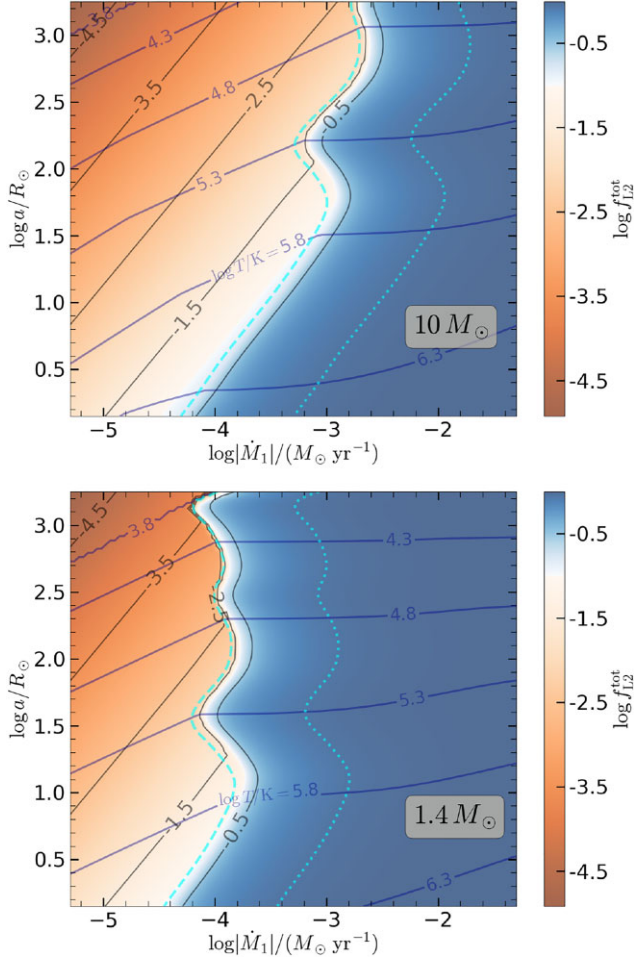


**Figure 3.** The total L2 mass-loss fraction (equation 34) from the binary system for different mass transfer rates  $|\dot{M}_1|$  and semimajor axes  $a$ , including contributions from the inner ( $f_{L2}^{\text{inner}}$ ) and outer ( $f_{L2}^{\text{outer}}$ ) disc. Here, we assume that the accretor is a compact object. The colour-shading and black contours show  $\log_{10} f_{L2}$ , and the dark blue contours show the gas temperature in the outer disc near  $R_d$ . The upper panel is for secondary mass  $M_2 = 10 M_\odot$  (BH), and the lower panel is for  $M_2 = 1.4 M_\odot$  (NS). For both panels, we have fixed the mass ratio  $q = M_2/M_1 = 0.5$  and viscosity parameter  $\alpha = 0.1$ . The gas composition is H-rich at solar metallicity ( $X = 0.7$ ,  $Z = 0.02$ ). The cyan dashes and dotted lines in each panel indicate where  $(Q_{\text{adv}} + Q_{L2})/Q_{\text{rad}} = 0.1$  and 1, respectively.

tends to cause the orbit to shrink faster or expand less than in the case without L2 mass-loss (e.g. van den Heuvel & De Loore 1973).

In the centre of mass frame, the specific angular momentum of the gas corotating at the L2 point is given by

$$\ell_{L2} = \Omega a^2 (x_{L2} - \mu)^2. \quad (35)$$

In the following, we assume that the asymptotic angular momentum of the gas escaping from the L2 nozzle is  $g_b \ell_{L2}$ , where  $g_b$  is a factor of order unity describing the angular momentum gain due to the torque from binary. Hydrodynamic simulations by Pejcha et al. (2016b, their Fig. 10) showed that the angular momentum gain is rather modest  $g_b \in (1, 1.3)$ . If the gas flowing out from the L2 point stays bound to the binary and forms an ‘decretion’ disc, then the long-term viscous evolution of the disc may further extract angular momentum from the binary and hence may lead to a higher effective  $g_b$  that is not captured by the simulations by Pejcha et al. (2016b). On the other hand, at extremely high mass-transfer rates such that  $f_{L2} \sim 1$ , the

L2 mass-loss may not achieve corotation with the orbit at the L2 point (see MacLeod et al. 2018b), so we may expect  $g_b < 1$  in such cases. Detailed numerical simulations would be required to carefully determine  $g_b$ .

When a fraction  $f_{L2} \approx f_{L2}^{\text{outer}}$  (ignoring  $f_{L2}^{\text{inner}}$ ) of the transferred mass  $\dot{M}_1$  is lost through the L2 nozzle, the angular momentum loss rate from the binary is given by

$$\dot{J}_{L2} = -f_{L2} |\dot{M}_1| g_b \ell_{L2}. \quad (36)$$

As we show later (equation 45), in the limit  $f_{L2} \approx 1$ , the orbital separation shrinks as long as  $g_b$  exceeds a critical  $g_{b,c} = 0.5\mu(1 + \mu)/(x_{L2} - \mu)^2$ , which is in the range  $0.1 \lesssim g_{b,c} \lesssim 0.4$  for  $0.3 < q < 3$ . Thus, the general effect of  $\dot{J}_{L2}$  is to push the two stars closer to each other.

When there is a large dynamical range between the surface or innermost stable circular orbit (ISCO) of the secondary  $R_2$  and the spherization radius  $R_{\text{sph}}$ , then the accretion disc is expected to take a self-similar or power-law (Blandford & Begelman 1999) radial profile of mass accretion rate in the radius range  $R_2 < R < R_{\text{sph}}$ ,

$$\dot{M}_{\text{acc}}(R) \simeq (R/R_{\text{sph}})^p (1 - f_{L2}) |\dot{M}_1|, \quad (37)$$

where the power-law index  $p$  is in general between 0 (no wind) and 1 (the maximum allowed by energy conservation). Numerical simulations of hot accretion flows typically find  $p \in (0.3, 0.8)$ , but this is still rather uncertain (see Yuan & Narayan 2014, and references therein). The basic result is that, if the size of the secondary is small  $R_2 \ll R_{\text{sph}}$  (e.g. in the case of a compact object), then only a very small fraction of the transferred mass is actually accreted onto the secondary,

$$\dot{M}_2 \equiv \dot{M}_{\text{acc}}(R_2) = \min[(R_2/R_{\text{sph}})^p, 1] (1 - f_{L2}) |\dot{M}_1|. \quad (38)$$

We assume that the wind directly escapes from the system in a quasi-spherical manner due to its fast speed (ignoring the small fraction that is recaptured by the binary’s potential). The angular momentum carried away by the wind has two components due to the Keplerian rotation at the disc surface and orbital motion of the secondary. The specific angular momentum of the wind, averaged over the total wind mass-loss rate of  $(1 - f_{L2}) |\dot{M}_1| - \dot{M}_2$ , is given by an integral over the Keplerian angular momentum profile  $\ell_K(R) = \sqrt{GM_2 R}$  over the entire disc,

$$\begin{aligned} \ell_w &= \frac{\int_{R_2}^{R_{\text{sph}}} dR (d\dot{M}_{\text{acc}}/dR) \sqrt{GM_2 R}}{(1 - f_{L2}) |\dot{M}_1| - \dot{M}_2} + \ell_2 \\ &= \frac{2p}{2p+1} \frac{1 - (R_2/R_{\text{sph}})^{p+1/2}}{1 - (R_2/R_{\text{sph}})^p} \sqrt{GM_2 R_{\text{sph}}} + \ell_2, \end{aligned} \quad (39)$$

where the accretion rate profile  $\dot{M}_{\text{acc}}(R)$  is given by equation (37) and

$$\ell_2 = \Omega a^2 (1 - \mu)^2 = (1 + q)^{-2} \sqrt{G(M_1 + M_2) a} \quad (40)$$

is the specific angular momentum of the secondary. The accretion onto the secondary also gives an angular momentum loss rate of  $\dot{M}_2 \sqrt{GM_2 R_2}$ , which is usually negligible unless the accretion rate is low or the secondary radius is large such that  $R_2 \sim R_{\text{sph}}$ . The ‘isotropic re-emission’ prescription often adopted in binary evolution studies (Paxton et al. 2015) corresponds to an assumption of  $\ell_w \approx \ell_2$ , which is only applicable if  $\sqrt{q(1+q)^3} R_{\text{sph}}/a \ll 1$ . We caution that this assumption is violated if  $R_{\text{sph}}$  is a sizable fraction of  $R_d$  (achieved at high mass-transfer rates) and  $q \gtrsim 2$ . Various specific angular momenta are shown in Fig. 4.

In the following, we ignore the small angular momentum contributions by the spins of the two stars. The total angular momentum

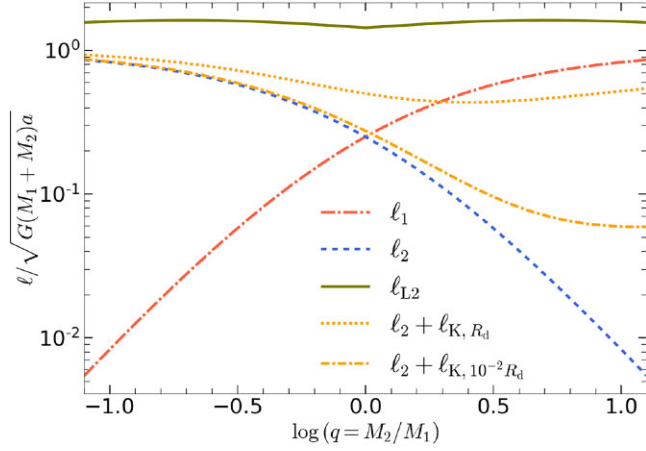


**Figure 4.** The specific angular momenta  $\ell_1$  (donor’s orbital motion, red long-dash-dotted line),  $\ell_2$  (accretor’s orbital motion, blue dashed line),  $\ell_{L2}$  (L2 point at corotation, green solid line),  $\ell_2 + \ell_K(R_d)$  (accretor’s orbital motion plus disc Keplerian rotation at the circularization radius  $R_d$ , orange dotted line),  $\ell_2 + \ell_K(10^{-2}R_d)$  (accretor’s orbital motion plus disc Keplerian rotation at a distance  $10^{-2}R_d$  from the accretor, orange short dash-dotted line), all in units of the specific orbital angular momentum per unit reduced-mass  $\sqrt{G(M_1 + M_2)a} = \Omega a^2$ . This shows that L2 mass-loss generally carries much more angular momentum per unit mass away from the binary system than other channels such as fast stellar wind (red/blue lines) or disc wind (orange lines).

loss rate of the binary system is

$$\dot{J} = \dot{J}_{L2} + \dot{J}_w, \quad (41)$$

where

$$\dot{J}_w = -[(1 - f_{L2})|\dot{M}_1| - \dot{M}_2] \ell_w. \quad (42)$$

Since the total mass-loss rate is  $\dot{M} = \dot{M}_1 + \dot{M}_2$ , we make use of the expression for total angular momentum of a Keplerian circular orbit  $J = \Omega a^2 M_1 M_2 / M$  ( $M$  being the total mass), and obtain the orbital shrinking (or expanding) rate

$$\frac{\dot{a}}{a} = 2 \frac{\dot{J}}{J} - 2 \frac{\dot{M}_1}{M_1} - 2 \frac{\dot{M}_2}{M_2} + \frac{\dot{M}}{M}. \quad (43)$$

In the limit, where the secondary is a compact object,  $(R_2/R_{\text{sph}})^p \ll 1$ ,  $\dot{M}_2 \ll |\dot{M}_1|$ , and  $\dot{M} \approx \dot{M}_1$ , we obtain

$$\frac{\dot{J}}{J} \approx \frac{\dot{M}_1}{\mu \dot{M}_1} \left\{ g_b f_{L2} (x_{L2} - \mu)^2 + (1 - f_{L2}) \left[ (1 - \mu)^2 + \frac{2p}{2p+1} \sqrt{\frac{\mu R_{\text{sph}}}{a}} \right] \right\}, \quad (44)$$

and hence

$$\begin{aligned} \xi &= \frac{\dot{a} \dot{M}_1}{a \dot{M}_1} \\ &\approx -(1 + \mu) + \frac{2}{\mu} \left\{ g_b f_{L2} (x_{L2} - \mu)^2 + (1 - f_{L2}) \left[ (1 - \mu)^2 + \frac{2p}{2p+1} \sqrt{\frac{\mu R_{\text{sph}}}{a}} \right] \right\}. \end{aligned} \quad (45)$$

In Fig. 5, we show the ratio between the dimensionless orbital shrinking rate  $\dot{a}/a$  and the mass-loss rate  $\dot{M}_1/M_1$  as a function of mass ratio  $q$  and  $f_{L2}$ , for  $g_b = 1$  (the L2 mass-loss carrying the corotational angular momentum of the L2 point). Here, we ignore the disc-rotational angular momentum component of the wind by

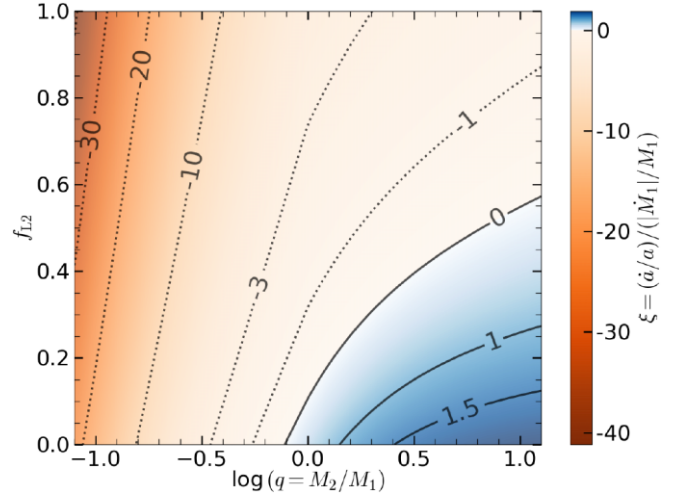


**Figure 5.** The ratio between the dimensionless orbital shrinking rate and the mass-loss rate,  $\xi = (\dot{a}/a)/(|\dot{M}_1|/M_1)$ , as a function of binary mass ratio  $q$  and the total L2 mass-loss fraction  $f_{L2}$ , according to equation (45). The binary orbit shrinks (or expands) when  $\xi < 0$  (or  $\xi > 0$ ). It is assumed that the L2 mass-loss carries the corotational angular momentum at the L2 point (taking  $g_b = 1$  in equation 36), and the disc-rotational component of the wind angular momentum is ignored (taking the limit of  $R_{\text{sph}} \ll a$ ). The secondary is taken to be a compact object with negligible accretion rate ( $\dot{M}_2 = 0$ ). We see that for  $q \lesssim 1/3$  (the donor is much more massive), the orbit rapidly shrinks on a time-scale that is many times shorter than the mass-loss time-scale  $M_1/|\dot{M}_1|$  of the primary. For  $q \gtrsim 1$  (the donor is less massive), the orbit may shrink as a result of significant L2 mass-loss, as opposed to the usual expectation of orbital expansion under  $f_{L2} = 0$ .

imposing  $R_{\text{sph}} \ll a$ . The qualitative effects of  $f_{L2}$  are unaffected by the choice of  $R_{\text{sph}}/a$ .

We find that, if  $q \lesssim 1/3$  and  $f_{L2} \simeq 1$ , the orbit rapidly shrinks on a time-scale that is a few to 10 per cent of the mass-loss time-scale of the primary,  $M_1/|\dot{M}_1|$ . Moreover, at sufficiently high mass-transfer rates such that  $f_{L2} \gtrsim 0.5$ , the orbit always shrinks for practically all mass ratios. Note that, under the (in our opinion questionable) assumptions of  $f_{L2} = 0$  and  $R_{\text{sph}}/a = 0$ , our equations (44) and (45) reduce to the conventional picture where the orbit starts to expand when  $q > 0.781$  (Postnov & Yungelson 2014). Faster orbital shrinking due to L2 mass-loss ( $f_{L2} \neq 0$ ) has implications for the formation of compact binary gravitational wave sources, which will be discussed in a companion paper.

#### 4 IR EXCESS FROM CIRCUMBINARY OUTFLOW

In this section, we discuss the radiative appearance of the L2 mass-loss, which is assumed to be in the form of a circumbinary outflow<sup>3</sup> (CBO). The physical picture is that the inner disc drives a quasi-spherical fast wind and the UV radiation escaping from the wind photosphere is reprocessed into IR emission by the CBO. A schematic picture is shown in Fig. 6.

Let us consider the case that a fraction  $f_{L2} \approx f_{L2}^{\text{outer}}$  of the mass transfer-rate  $|\dot{M}_1|$  is channeled into the CBO and the rest  $(1 - f_{L2})$  is driven away as a quasi-spherical wind. The scattering photosphere

<sup>3</sup>For a wide range of mass ratios  $0.06 \lesssim q(\text{or } q^{-1}) \lesssim 0.8$ , cold gas streaming out from the L2 nozzle gains energy from the binary’s tidal torque and becomes unbound (Shu et al. 1979; Pejcha et al. 2016b).



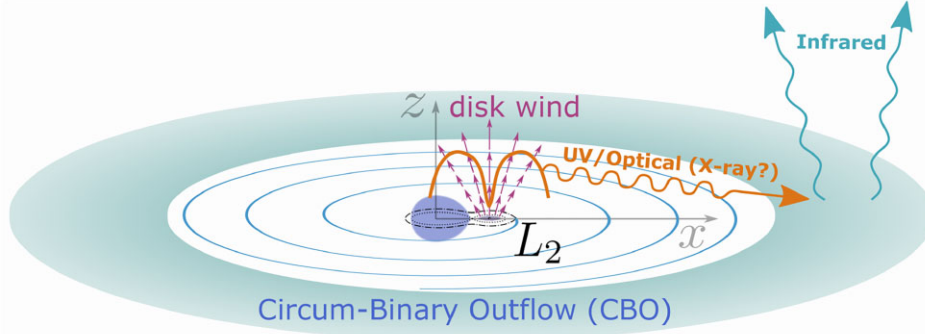


**Figure 6.** Schematic picture of a binary system undergoing mass transfer at a high rate greater than  $10^{-4} M_{\odot} \text{ yr}^{-1}$  such that a significant fraction of the transferred mass is lost through the L2 point, forming a circumbinary outflow (CBO). Immediately after flowing out from the L2 nozzle, the gas is in the form of a spiral-shaped supersonic cold stream. At large distances (5 to 10 times the semimajor axis) from the binary, the gas undergoes internal shocks and forms an axisymmetric geometrically thin outflow. The inner accretion disc near the accretor launches a fast wind whose scattering photosphere is indicated by a thick orange curve. The UV/optical (and a small flux of X-ray) photons from the hot photosphere irradiate the CBO, which reprocesses the incident radiation into longer wavelength photons in the infrared (IR) bands. This model explains the IR excess observed in some ULXes (e.g. Lau et al. 2019).

of the wind is located at radius

$$R_s = \frac{(1 - f_{L2})|\dot{M}_1|\kappa_s}{4\pi v_w} \\ = 0.4 \text{ AU} \frac{\kappa_s}{0.34 \text{ cm}^2 \text{ g}^{-1}} \frac{(1 - f_{L2})|\dot{M}_1|}{10^{-3} M_{\odot} \text{ yr}^{-1}} \frac{0.01c}{v_w}, \quad (46)$$

where we have taken a scattering opacity  $\kappa_s \equiv 0.34 \text{ cm}^2 \text{ g}^{-1}$  for H-rich composition and the wind velocity  $v_w$  is set by the spherization radius (where most of the disc outflow originates, Begelman et al. 2006)

$$v_w \sim \sqrt{\frac{GM_2}{R_{\text{sph}}}} = \sqrt{\frac{L_{\text{Edd},2}}{(1 - f_{L2})|\dot{M}_1|}}. \quad (47)$$

For high mass accretion rates  $(1 - f_{L2})|\dot{M}_1| \sim 10^{-3} M_{\odot} \text{ yr}^{-1}$ , the wind velocity is about  $10^{-2} c$  and the wind photospheric radius can be comparable to or larger than the orbital separation. This makes it difficult to observe the donor star.

The luminosity and spectrum of the radiation escaping from the wind depend on the nature of the accretor as well as the viewing angle. In the case of a compact-object accretor (BH or NS), the bolometric luminosity of the entire system is dominated by the innermost regions of the accretion disc. Only a small fraction of the transferred mass reaches near the ISCO (equation 37), so photons decouple from the gas within ten times the ISCO radii even though the wind velocity is close to the speed of light (Jiang, Stone & Davis 2014, 2019). From viewing angles not far from the rotational axis of the disc, the system is expected to appear as a bright ULX source with X-ray luminosity  $L_X > 10^{39} \text{ erg s}^{-1}$  (Kaaret et al. 2017). However, due to geometric beaming (Narayan, Sądowski & Soria 2017), the X-ray photons from the fastest wind do not reach the CBO which is located near the equatorial plane.

Instead, the irradiation of the CBO is dominated by the photons that are reprocessed by the wind launched from near the spherization radius  $R_{\text{sph}}$  and then escape at the scattering photosphere given by equation (46). Hereafter, we denote the luminosity and colour temperature of the radiation escaping from the scattering photosphere of the wind as  $L_s$  and  $T_s$ . We expect  $L_s$  to be comparable to (or perhaps slightly higher than) the Eddington luminosity  $L_s \sim L_{\text{Edd},2} \sim 10^{38} (M_2/M_{\odot}) \text{ erg s}^{-1}$ , whereas the temperature  $T_s$  is set by the radius of the last-absorption  $R_{\text{th}}$ , where the effective/thermalization optical

depth is unity (Rybicki & Lightman 1986, their equation 1.120)

$$\tau_{\text{eff}} = \sqrt{3\kappa_a(\kappa_a + \kappa_s)\rho_w R_{\text{th}}} \simeq 1, \quad (48)$$

where  $\kappa_a$  is the absorption opacity for photons near the peak of the local spectral energy distribution (SED) and  $\kappa_s$  is the scattering opacity. The opacity depends on the wind density  $\rho_w = (1 - f_{L2})|\dot{M}_1|/(4\pi R^2 v_w)$  as well as the local intensity/spectrum of the radiation field. In the limit  $\kappa_a \ll \kappa_s$ , the Rosseland-mean optical depth ( $\sim$ scattering optical depth) at  $R_{\text{th}}$  is  $\tau(R_{\text{th}}) \simeq R_s/R_{\text{th}} \simeq \sqrt{\kappa_s/3\kappa_a}$ , and the luminosity of the escaping photons is given by

$$L_s \simeq 4\pi R_{\text{th}}^2 \frac{a_r T_s^4 c}{\tau} \simeq 4 \left( \frac{3\kappa_a}{\kappa_s} \right)^{3/2} (4\pi R_s^2 \sigma_{\text{SB}} T_s^4), \quad (49)$$

where  $\sigma_{\text{SB}} = a_r c/4$  is the Stefan–Boltzmann constant. Therefore, we obtain a rough estimate of the colour temperature of the radiation escaping from the wind

$$T_s \simeq 2.5 \times 10^4 \text{ K} \left( \frac{L_s}{10^{39} \text{ erg s}^{-1}} \right)^{1/4} \left( \frac{\kappa_a}{0.01 \text{ cm}^2 \text{ g}^{-1}} \right)^{-3/8} \\ \left( \frac{\kappa_s}{0.34 \text{ cm}^2 \text{ g}^{-1}} \right)^{-1/8} \left( \frac{(1 - f_{L2})|\dot{M}_1|}{10^{-3} M_{\odot} \text{ yr}^{-1}} \right)^{-1/2} \left( \frac{v_w}{0.01c} \right)^{1/2}. \quad (50)$$

It is beyond the scope of this paper to solve the full frequency-dependent radiative transport problem throughout the wind (see Shen et al. 2015, for general considerations). Our preliminary calculations based on CLOUDY<sup>4</sup> showed that, for the fiducial parameters above, the bound-free absorption opacity near photon energy  $3k_B T_s \sim 10 \text{ eV}$  ( $T_s/3 \times 10^4 \text{ K}$ ) is of the order  $10^{-2} \text{ cm}^2 \text{ g}^{-1}$  at  $R_{\text{th}}$  (where the scattering optical depth is  $\sim 3$ ). Since the wind velocity scales as  $v_w \propto [(1 - f_{L2})|\dot{M}_1|]^{-1/2}$  (equation 47) and the absorption opacity  $\kappa_a$  generally decreases with accretion rate, we see that the photospheric temperature is a decreasing function of the mass accretion rate – bright emission in the optical band is only possible at high accretion rates.

Observationally, a large fraction of ULXes have optical counterparts (e.g. Tao et al. 2011; Gladstone et al. 2013; Vinokurov, Fabrika & Atapin 2018) and the brightest ones have spectral luminosity of  $\nu L_{\nu} \sim 10^{38} \text{ erg s}^{-1}$  in the *B* band (e.g. Holmberg II X-1, Holmberg IX X-1, M101 ULX-1). These sources with

<sup>4</sup>Version 17.01 of the code last described by Ferland et al. (2017).

brightest optical luminosities are consistent with the emission from the aforementioned wind with  $L_s \sim 10^{39} \text{ erg s}^{-1}$  and  $T_s \simeq 3 \times 10^4 \text{ K}$ . Follow-up observations of some of these sources show that the flux density at longer wavelengths (near- and mid-IR) is much higher than the simple power-law extrapolation from the optical bands (Heida et al. 2014; López et al. 2017; Lau et al. 2017, 2019). In the following, we show that the IR excess is consistent with the reprocessed emission from the CBO.

Let us consider the CBO to be a geometrically thin but optically thick sheet near the orbital plane of the binary and that the CBO extends from an inner radius  $R_{\min}$  to outer radius  $R_{\max}$ . The L2 mass-loss flows out in the form of a supersonic thin spiral-shaped stream, which then undergoes internal shocks and forms an axisymmetric outflow at a distance 5 to 10 times the binary separation (Pejcha, Metzger & Tomida 2016a; Pejcha et al. 2016b). Thus, the inner radius of the reprocessing sheet is at

$$R_{\min} \sim 10a. \quad (51)$$

In the test particle limit (as considered by Shu et al. 1979), the motion of a fluid element initially corotating at the L2 point is controlled by the binary's tidal torque, and it can acquire positive energy with asymptotic speed  $0 < v_{\text{eq}} \lesssim (1/3)\sqrt{GM/a}$  ( $M$  being the total mass) provided that the mass ratio is  $q \lesssim 0.8$  or  $q \gtrsim 1.3$ . The importance of pressure effects have been studied by Pejcha et al. (2016b), Hubová & Pejcha (2019), who found that if the gas leaving the L2 point has significant thermal energy and is radiatively inefficient, then the radial pressure gradient can accelerate the gas to a higher asymptotic speed than in the test particle limit. Having these uncertainties in mind, we take

$$v_{\text{eq}} \simeq \frac{1}{3} \sqrt{\frac{GM}{a}} \simeq 46 \text{ km s}^{-1} \left( \frac{M}{10M_{\odot}} \right)^{\frac{1}{2}} \left( \frac{a}{100R_{\odot}} \right)^{-\frac{1}{2}}. \quad (52)$$

The vertical extent of the CBO also depends on the thermal energy at the L2 point. In the following, we adopt a fiducial value for the height-to-radius ratio,  $f_{\Omega} \equiv H/R = 0.1f_{\Omega, -1}$ . Therefore, the density profile of the CBO is given by

$$\rho_{\text{eq}}(R) = \frac{f_{\text{L2}} |\dot{M}_1|}{4\pi f_{\Omega} R^2 v_{\text{eq}}}. \quad (53)$$

The outer radius  $R_{\max}$  is bounded by the age of the CBO ejection  $v_{\text{eq}} t_{\text{age}} \sim 10^{17} \text{ cm}$  ( $v_{\text{eq}}/50 \text{ km s}^{-1}$ ) ( $t_{\text{age}}/10^3 \text{ yr}$ ). Another important constraint is the *radial* optical depth for incident photons  $\tau_{\text{eq}}(R) = \rho_{\text{eq}} \kappa_{\text{P}} R$ , where  $\kappa_{\text{P}}$  is the Planck-mean opacity of the photoionized region of the CBO (our fiducial opacities below are estimated based on CLOUDY simulations). If  $\tau_{\text{eq}} < 1$ , the CBO is no longer an efficient reprocessor, and hence the maximum radial extent is set by  $\tau_{\text{eq}}(R_{\max}) = 1$ , i.e.

$$R_{\max} = \frac{f_{\text{L2}} |\dot{M}_1| \kappa}{4\pi f_{\Omega} v_{\text{eq}}} \simeq 1 \times 10^{16} \text{ cm} \frac{\kappa_{\text{P}}}{1 \text{ cm}^2 \text{ g}^{-1}} \frac{f_{\text{L2}} |\dot{M}_1|}{10^{-3} M_{\odot} \text{ yr}^{-1}} \frac{50 \text{ km s}^{-1}}{v_{\text{eq}}} \frac{0.1}{f_{\Omega}}. \quad (54)$$

At radii  $R_{\min} < R \ll R_{\max}$ , only a thin surface layer of the CBO is directly irradiated by the source photons (Chiang & Goldreich 1997), whereas at much larger radii  $R \gg R_{\max}$ , the entire CBO is photoionized by the UV photons from the disc wind. The photoionized regions have temperature  $T \sim 10^4 \text{ K}$  (as given by the balance between photoelectric heating and cooling due to collisional excitation, Draine 2011) and isothermal sound speed  $c_s \simeq \sqrt{1.5k_{\text{B}}T/m_{\text{p}}} \simeq 10(T/10^4 \text{ K}) \text{ km s}^{-1}$ , so the gas undergoes vertical expansion to reach a height-to-radius ratio of  $c_s/v_{\text{eq}} \sim 0.2$ .

The vertical expansion reduces the density as compared to that in equation (53) and hence,  $R_{\max}$  should be self-consistently reduced. More physically, the low-density gas at a few scale-heights away from the mid-plane is heated to higher temperatures close to  $T_s$  and expands faster in the vertical direction. Some of the vertically extended gas may also interact with the fast disc wind (via a turbulent shearing layer), which may cause the entire CBO to evaporate. In the following, we only consider the region  $R \ll R_{\max}$ , where the bulk of the CBO can be considered as a dynamically cold gas sheet.

The flux received by the reprocessing sheet at radius  $R \in (R_{\min}, R_{\max})$  is given by the following integral

$$F(R) = I_s R_s^2 \int_0^{\theta_s} \sin \theta d\theta \int_{-\pi/2}^{\pi/2} d\phi \frac{(R \cos \theta - R_s) R_s \sin \theta \cos \phi}{(R^2 + R_s^2 - 2RR_s \cos \theta)^2} \\ = I_s \left( \frac{R_s}{R} \right)^3 \int_0^{\theta_s} d\theta \frac{2(\cos \theta - R_s/R) \sin^2 \theta}{[1 - 2(R_s/R) \cos \theta + R_s^2/R^2]^2}, \quad (55)$$

where  $\theta$  and  $\phi$  are the polar and azimuthal angles in a spherical coordinate system with the origin at the centre of the photosphere, polar axis pointing in the direction of a surface element on the reprocessing sheet, and the sheet lying in the  $\phi = \pm\pi/2$  plane. We have also defined  $\theta_s = \cos^{-1}(R_s/R)$  as the maximum polar angle contributing to the incoming flux and  $I_s = \int dv I_{s,v}$  as the frequency-integrated intensity at the wind photosphere. The angular dependence of the intensity is taken to be isotropic at the photosphere, whereas in reality, this is affected by limb darkening (which would change the results at an order-unity level).

For simplicity, let us assume that the photospheric emission has a blackbody spectrum at temperature  $T_s$ , meaning that

$$I_{s,v} = D_s B_v(T_s), \quad \pi I_s = D_s \sigma_{\text{SB}} T_s^4, \quad (56)$$

where  $B_v(T) = 2h\nu^3 c^{-2} (e^{h\nu/k_{\text{B}}T} - 1)^{-1}$  ( $h$  being the Planck constant) is the Planck function and we have defined a dilution factor  $D_s$  based on equation (49),

$$D_s \equiv \frac{L_s}{4\pi R_s^2 \sigma_{\text{SB}} T_s^4} = 4 \left( \frac{3\kappa_a}{\kappa_s} \right)^{3/2} < 1. \quad (57)$$

At radii  $R \ll R_{\max}$ , only a thin surface layer with  $\Delta H/H \ll 1$  is photoionized and the gas density in the surface layer is much less than that at the equatorial plane. Depending on the detailed vertical density profile (which determines the ratio between absorption and scattering opacity at different heights), this surface layer has an albedo  $0 < \varpi < 1$ , where the upper (or lower) limit corresponds to a scattering (or absorption) dominated surface layer. The net result is that a fraction  $1 - \varpi$  of the flux is absorbed by the CBO, and we assume that this amount of energy is re-emitted as a blackbody at the local effective temperature given by

$$\sigma_{\text{SB}} T_{\text{eff}}^4(R) = (1 - \varpi) F(R), \quad (58)$$

whereas the rest of the incident flux  $\varpi F(R)$  is reflected away from the CBO. Physically, the albedo  $\varpi$  is expected to be a (mildly) decreasing function of radius, because the fractional height  $\Delta H/H$  of the photoionized layer increases with radius, and this leads to a decrease in the ionization parameter (which is defined as the ratio between the incident photon number density and the gas number density). For the purpose of obtaining rough estimates for the reprocessed emission, we simply adopt a constant  $\varpi$  throughout the entire range of radii.

In the limit  $R \gg R_s$ , we have  $F \propto R^{-3}$  and the effective temperature of the re-emission scales as  $T_{\text{eff}} \propto R^{-3/4}$ . Since  $T_{\text{eff}}$  is proportional to the peak emission frequency from each annulus, this generates a power-law spectrum  $L_{\nu} \propto dL/dT_{\text{eff}} \propto d(R^2 F)/dT_{\text{eff}} \propto \nu^{1/3}$ , which

is much shallower than the Rayleigh–Jeans slope. This power law truncates at radius  $R_{\max}$  (the shape of the spectrum at  $\nu \ll \nu_{\min}$  depends on the emission from the photoionized gas at  $R \gtrsim R_{\max}$ ), which means the spectrum below  $\nu_{\min} \simeq (R_{\max}/R_s)^{-3/4} k_B T_s/h$  will be Rayleigh–Jeans-like (however, free-free emission from the photoionized gas will dominate at  $\nu \ll \nu_{\min}$ , which we do not consider here). Note that, if the equatorial outflow has a flared structure (i.e. height-to-radius ratio increasing with radius) or the albedo  $\varpi$  decreases with radius, then the re-emission at longer wavelengths is enhanced compared to our calculation (Chiang & Goldreich 1997).

For a line-of-sight inclination angle of  $\Theta_{\text{obs}}$  wrt. the rotational axis of the system, the isotropic equivalent specific luminosity at frequency  $\nu$  is given by

$$L_\nu = 4\pi^2 R_s^2 I_{s,\nu} + 4\pi \cos \Theta_{\text{obs}} \int_{R_{\min}}^{R_{\text{eq}}} \left[ B_\nu(T_{\text{eff}}) + \frac{\varpi F(R)}{\sigma_{\text{SB}} T_s^4} B_\nu(T_s) \right] 2\pi R dR, \quad (59)$$

where the first term is the contribution from the wind photosphere itself, and the second term has a cold thermal ( $T_{\text{eff}}$ ) component from deeper layers close to the mid-plane and a hot reflected component ( $T_s$ ) from the photoionized surface layer. Then equations (55) and (59) can be re-written in the following dimensionless forms

$$\tilde{F}(x) \equiv \frac{F(R)}{\pi I_s} = \frac{2}{\pi} \int_{x^{-1}}^1 d\tilde{\mu} \frac{(x\tilde{\mu} - 1)\sqrt{1 - \tilde{\mu}^2}}{(x^2 + 1 - 2x\tilde{\mu})^2}, \quad (60)$$

and

$$\tilde{L}_\nu \equiv \frac{L_\nu}{4\pi^2 R_s^2 I_{s,\nu}} = 1 + 2 \cos \Theta_{\text{obs}} \times \int_{x_{\min}}^{x_{\max}} dx \left[ D_s^{-1} \frac{e^{h\nu/k_B T_s} - 1}{e^{h\nu/k_B T_{\text{eff}}} - 1} + \varpi D_s \tilde{F}(x) \right], \quad (61)$$

where  $x = R/R_s$ ,  $x_{\min} = R_{\min}/R_s$ ,  $x_{\max} = R_{\max}/R_s$ , and  $T_{\text{eff}}(x)/T_s = [(1 - \varpi)D_s \tilde{F}(x)]^{1/4}$ .

The spectra of the reprocessing system are shown in Fig. 7 for two cases of different outer radii  $R_{\max}/R_s = 300$  and 30. We adopt the following parameters: wind luminosity  $L_s = 10^{39} \text{ erg s}^{-1}$ , source temperature  $T_s = 3 \times 10^4 \text{ K}$ , photospheric radius  $R_s = 0.5 \text{ AU}$ , inner CBO radius  $R_{\min} = 4R_s$ , albedo of the photoionized layer  $\varpi = 0.4$ , and observer's viewing angle  $\Theta_{\text{obs}} = \pi/6$ . These parameters are motivated by the consideration of a binary system with mass-transfer rate of the order  $10^{-3} M_\odot \text{ yr}^{-1}$ . We find that the IR luminosity from such a system is  $L_{\text{IR}} \sim 5 \times 10^{37} \text{ erg s}^{-1}$ . For lower  $|\dot{M}_1|$ , the source temperature  $T_s$  will be higher and the photospheric radius smaller, so the reprocessed IR luminosity will be lower. We note that the IR luminosity due to reprocessing is likely brighter than that generated by internal shocks within the CBO (Pejcha et al. 2016b)

$$L_{\text{sh}} \sim 0.03 f_{\text{L2}} \frac{GM|\dot{M}_1|}{a} \simeq 3 \times 10^{35} \text{ erg s}^{-1} \frac{f_{\text{L2}}|\dot{M}_1|}{10^{-3} M_\odot \text{ yr}^{-1}} \frac{M}{10 M_\odot} \frac{100 R_\odot}{a}. \quad (62)$$

Our model prediction is compared to the SED of a luminous ULX (with apparent X-ray luminosity  $L_X \sim 10^{40} \text{ erg s}^{-1}$ ) in the nearby dwarf star-forming galaxy Holmberg II, Holmberg II X-1 (e.g. Kaaret, Ward & Zezas 2004; Goad et al. 2006; Bergeha et al. 2010; Tao et al. 2012; Walton et al. 2015). This ULX has bright optical ( $U, B, I$  bands), near-IR (*Keck*  $H$  and  $K_s$  bands), and mid-IR (warm *Spitzer* IRAC 3.5 and 4.5  $\mu\text{m}$  bands) counterparts (Tao et al. 2011; Heida et al. 2014; Lau et al. 2017, 2019). The median is used if the flux at a given band has significant time variability. The IR flux greatly exceeds the extrapolation from the optical bands and has been

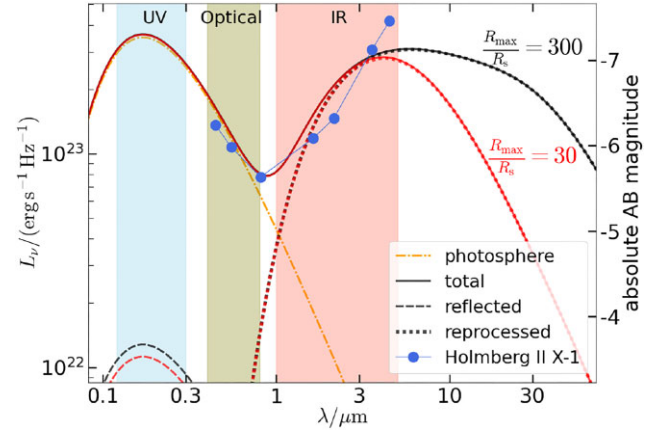


**Figure 7.** Spectra from a spherical photosphere and an optically thick circum-binary sheet in the equatorial plane, for two cases of different outer radii  $R_{\max}/R_s = 300$  (black) and 30 (red). For both cases, the inner radius of the equatorial sheet is  $R_{\min}/R_s = 4$  and the scattering photospheric radius is  $R_s = 0.5 \text{ au}$ . The emission emerging from the photosphere has luminosity  $L_s = 10^{39} \text{ erg s}^{-1}$  and is assumed to be a blackbody at temperature  $T_s = 3 \times 10^4 \text{ K}$  (orange dash-dotted line). The equatorial sheet has two emission components – reflected component from the photoionized hot surface (dashed lines) and reprocessed component from the deep interior (dotted lines) – and their relative contribution is given by the albedo  $\varpi = 0.4$ . The observer's viewing angle wrt. to the rotation axis is  $\Theta_{\text{obs}} = \pi/6$ . For comparison, we show the spectral energy distribution of Holmberg II X-1 (a bright ULX, see the text for references) where the IR excess is consistent with reprocessing by circumbinary material.

interpreted as the emission from circumstellar dust or a supergiant Be star by Lau et al. (2017, 2019). Here, our model provides a physical explanation of the bright IR emission being due to reprocessing by a CBO from L2 mass-loss. We do not provide a statistical fit to the SED of Holmberg II X-1, because the photometry in the near-IR (or mid-IR) was carried out with instruments with angular resolution of about 1 arcsec (or a few arcsec), and the contribution from diffuse emission and noise in the adopted aperture (of physical radii of 10 to 30 pc at the source distance) may be significant.

We also note that the brightest Galactic micro-quasar SS433 (see Fabrika 2004, for a review) is undergoing mass transfer at a rate that is estimated to be of the order  $10^{-4} M_\odot \text{ yr}^{-1}$  based on the mass outflow rate inferred from the infrared spectrum (Shkovskii 1981; van den Heuvel 1981) and its binary separation is  $a \simeq 60 R_\odot [(M_1 + M_2)/20 M_\odot]^{1/2}$  for an orbital period of 13.1 d. There is strong evidence for the existence of CBO in this system<sup>5</sup> (as initially suggested by Filippenko et al. 1988). However, since SS433 is close to the Galactic plane with high (and uncertain) dust extinction  $A_V \sim 8 \text{ mag}$  (Wagner 1986), we do not attempt to model the SED of this source here.

<sup>5</sup>The evidence includes (1) that the stationary  $H\alpha$  lines (and other recombination lines) have two narrow components that are blue-shifted and red-shifted with half-separation of about  $200 \text{ km s}^{-1}$  independent of the orbital revolution whereas the inner regions of the accretion disc undergo eclipses in each orbit – these two narrow components must come from circumbinary gas (Blundell et al. 2008); (2) the spatially resolved images of radio (free-free) emission shows outflowing gas in the equatorial plane roughly perpendicular to the jets (Paragi et al. 1999; Blundell et al. 2001); (3) near-IR interferometric observations shows that the low-velocity core of the stationary  $\text{Br}\gamma$  line is emitted by gas moving perpendicular to the jet directions (Waisberg et al. 2019).



Our model can also be applied to systems shortly before one of the stars undergoes a SN explosion. If a pre-SN system has strong L2 mass-loss, reprocessing of the UV and soft X-ray emission from the disc wind by the equatorial outflow should generate bright near-IR excess at the level of  $\sim 10$  per cent of the accretor's Eddington luminosity. This provides a possible explanation of the photometric detections of 'cool' progenitor systems of some SNe (Smartt 2015), because the equatorial outflow has a much larger surface area than that of the pre-explosion star. For instance, the Type Ib SN 2019yvr had archival multiband pre-explosion images at its position showing bright emission with  $\nu L_\nu \simeq 7 \times 10^{37} \text{ erg s}^{-1}$  at wavelength  $\lambda = 0.8 \mu\text{m}$  (Kilpatrick et al. 2021; Sun et al. 2021). This is consistent with reprocessing by a CBO but difficult to explain by a single hydrogen-poor star model. Moreover, SN 2019yvr transitioned into a Type IIn at late time with narrow H $\alpha$  emission line, X-ray, and radio emission from shock interaction with circumstellar material, further supporting our picture.

## 5 DISCUSSION

In this section, we discuss the limitations of our model, which may be improved in the future.

(1) The boundary between  $f_{L2} \ll 1$  and  $f_{L2} \sim 1$  in the  $|\dot{M}_1|$ - $a$  plane (Fig. 2) is affected by many factors that are explicitly contained in our model description. In the Appendix, we show how the results depend on the gas composition, which affects the Rosseland-mean opacity and hence the radiative cooling rate  $Q_{\text{rad}}$ . Generally, at lower opacities (e.g. for a hydrogen poor composition), higher mass-transfer rates are needed to trigger L2 mass-loss. The results also depend on the dimensionless viscosity parameter  $\alpha$  (fixed at fiducial value of 0.1) and mass ratio  $q = M_2/M_1$  (fixed at fiducial value of 0.5). We do not explore the entire multidimensional parameter space here in this paper. Instead, we make our source code public,<sup>6</sup> so it can be used to calculate the L2 mass-loss fraction for any set of parameters.

(2) The outer disc near radius  $R_d$  is described by a one-zone model based on global mass/energy conservation. Such a one-zone model is only a crude approximation of the full 3D structure of the accretion flow, and the quantitative results can only be trusted to within a factor of a few. More realistically, because the gas at different radii experiences different heating and cooling rates, the Bernoulli number is a function of radius and this radial dependence determines which part of the disc is susceptible to wind or L2 mass-loss. Moreover, if we consider the gas profile in the vertical direction, at radii, where radiative cooling is inefficient, the gas at higher latitudes tends to have a higher Bernoulli number and hence is escaping the disc more easily (Stone et al. 1999). Furthermore, a fraction of the gas is located near the tidal truncation radius (which is slightly smaller than the volume-equivalent Roche lobe radius of the secondary,  $R_{v,2}$ ) and their orbits are significantly non-circular. The assumption of Keplerian rotation breaks down. These multidimensional effects are better captured in (more expensive) numerical simulations (e.g. MacLeod et al. 2018b), which will be explored in the future.

(3) Our radiative cooling term  $Q_{\text{rad}}$  (equation 21) considers photon diffusion in a uniform gas, whereas more realistically, the gas density profile is likely highly inhomogeneous such that photons try to escape through the lower density regions along the paths of least resistance (Blaes et al. 2011; Jiang et al. 2014). If radiative cooling is more efficient than in our model, then the gas Bernoulli number is reduced

and hence a higher mass-transfer rate is needed to trigger L2 mass-loss.

(4) We focus on the case of stable mass transfer. The donor loses its envelope on a time-scale much longer than the dynamical time of  $\Omega^{-1}$  ( $\Omega$  being the binary orbital frequency). In the case of dynamically unstable mass transfer (e.g. right before a merger event), the assumption of corotation breaks down and our model provides a poor description for the hydrodynamics of the system. At extremely high mass-transfer rates  $|\dot{M}_1| \gtrsim 10^{-2} M_\odot \text{ yr}^{-1}$ , a fraction of the shock-heated gas with the highest Bernoulli number is likely lost on a dynamical time. This fraction of gas is unable to form an accretion disc and hence does not contribute to viscous heating. It is also likely that some of the high-Bernoulli-number gas is lost through the L3 nozzle. We speculate that the mass-loss from the system is still concentrated near the equatorial plane, but the height-to-radius ratio of the CBO likely increases with the mass-transfer rate.

(5) We have restricted our analysis to the case where the accretor's radius is less than the circularization radius of the incoming stream from the L1 nozzle ( $R_2 < R_d$ ). In many binary systems (e.g. double main-sequence or double white-dwarf), the two stars have similar radii such that  $R_2 > R_d$ , and hence the stream directly hits the surface of the accretor. At low mass-transfer rates, the mass transfer is conservative such that  $\dot{M}_2 = -\dot{M}_1$  (up to the point where the accretor is spun to near the critical rotation rate). However, for high mass-transfer rates such that  $G\dot{M}_2\dot{M}_1/R_2 > L_{\text{Edd},2}$ , the shocked gas is unable to radiatively cool ( $Q_{\text{rad}}^- \ll Q_{\text{sh}}^+$ ). The strong radiation pressure potentially pushes a fraction of the incoming gas (as well as some material originally from the accretor) away from the system through the L2 nozzle, and the rest of the gas settles down on the surface of the accretor. Thus, we still expect the formation of an equatorially concentrated CBO. The consequence of the rapid angular momentum loss associated with the L2 outflow is that the system is more likely to undergo a violent merger than in the case of conservative mass transfer. The merger ejecta interacts with the CBO and generates a bright transient in the optical band (Metzger & Pejcha 2017).

(6) We do not specify the physical origin of the high mass-transfer rates considered in this work. Due to their short lifetime ( $10^3$  to  $10^4$  yr) and the requirement of massive binary initial conditions, these systems are very rare in the Universe, with cosmic number density of the order  $10^8 \text{ Gpc}^{-3}$  or less. Despite their rarity, such systems may produce some of the most interesting sources in high-energy astrophysics: compact object mergers, stellar mergers, micro-quasars/ULXes, and interaction-powered SNe. Future binary population modelling is needed to identify possible evolutionary pathways that lead to the high mass-transfer rates.

## 6 SUMMARY

This paper considers the hydrodynamics of semidetached binary systems where the donor transfers mass to the companion via Roche lobe overflow. We construct a physical model for the accretion disc around the companion. It is proposed that, at sufficiently high mass-transfer rates such that the accretion flow becomes geometrically thick (or advection-dominated) near the outer disc radius, a large fraction of the transferred mass is lost through the L2 point. This is based on the physical intuition that losing mass from the L2 point is energetically favourable over lifting material to infinity by a fast wind.

Our model predicts the fraction of the transferred mass that is directly lost through the L2 nozzle from the outer disc  $f_{L2}^{\text{outer}}$ , which becomes of the order unity when  $|\dot{M}_1| \gtrsim \text{few} \times 10^{-4} M_\odot \text{ yr}^{-1}$ . Our

<sup>6</sup><https://github.com/wenbinlu/L2massloss.git>

model is tentatively supported by the (although inviscid) hydrodynamic numerical simulations by MacLeod et al. (2018a, b), who studied binary systems undergoing unstable mass transfer (at a rate of the order  $10^{-2} M_{\odot} \text{ yr}^{-1}$  or higher) and identified mass-loss through the L2 point (as well as the L3 point). Future MHD simulations taking into account viscous accretion are needed to further test our model.

At lower mass-transfer rates  $|\dot{M}_1| \lesssim 10^{-4} M_{\odot} \text{ yr}^{-1}$ , when direct L2 mass-loss from the outer disc is negligible ( $f_{\text{L2}}^{\text{outer}} \approx 0$ ), the inner disc can launch a strong outflow near the spherization radius  $R_{\text{sph}}$  where the accretion luminosity approaches the Eddington limit of the accretor, provided that the size of the accretor is small (e.g. in the case of a compact object). In this case, the majority of the disc wind directly leaves the system at a typical speed  $v_w \sim \sqrt{GM_2/R_{\text{sph}}}$ , whereas a small fraction of (or the slowest part of) the wind can still be captured by the equipotential surfaces passing near the L2 point. We estimate the L2 mass-loss fraction from the inner disc to be  $f_{\text{L2}}^{\text{inner}} \sim |\Phi_{\text{L2}}|/(GM_2/R_{\text{sph}})$  and we find it to be small:  $f_{\text{L2}}^{\text{inner}}$  is at most a few per cent at low mass-transfer rates  $|\dot{M}_1| \lesssim 10^{-4} M_{\odot} \text{ yr}^{-1}$ .

Material leaving the binary system via the L2 point forms a circumbinary outflow (CBO), although it is also possible to produce a decretion disc for a narrow range of binary mass ratio  $0.8 \lesssim q \lesssim 1.3$  (Shu et al. 1979). Due to the large lever-arm of the L2 point, a large L2 mass-loss fraction may cause rapid angular momentum loss, which tends to shrink the orbital separation, leading to shorter orbital periods or potentially unstable mass transfer. The effects on binary evolution and merger rates of gravitational wave sources will be explored in a companion paper with MESA (Paxton et al. 2019) simulations.

A key signature of a system undergoing L2 mass-loss is that the UV/optical emission from the hot accretion disc wind is reprocessed by the CBO into the IR bands. This produces an IR luminosity that can reach about 10 per cent of the Eddington luminosity of the accretor. Thus, we encourage taking high-resolution images of nearby ULXes with the **JWST** to identify possible IR counterparts and measure their IR fluxes. Another implication of our model is that, if a binary had L2 mass-loss before the SN explosion of one of the stars, then the pre-SN system (if detected in archival images) should have an IR excess due to reprocessing by the CBO. This provides a possible explanation of the ‘cool progenitor’ of Type Ib SN 2019yvr (Kilpatrick et al. 2021).

## ACKNOWLEDGEMENTS

We thank Nadia Zakamska, Jim Stone, Alexey Bobrick, and Pablo Marchant for useful conversations. We are grateful for the careful read and detailed comments made by the referee, Christopher Tout. WL was supported by the David and Ellen Lee Fellowship at California Institute of Technology and the Lyman Spitzer, Jr. Fellowship at Princeton University. This project has received funding from the European Union’s Horizon 2020 research and innovation programme under the Marie Skłodowska-Curie grant agreement No 836751.

## DATA AVAILABILITY

The data underlying this article will be shared on reasonable request to the corresponding author.

## REFERENCES

Abbott R. et al., 2020, *ApJ*, 913, L41  
Abbott R. et al., 2021, *Phys. Rev. X*, 11, 021053

- Abramowicz M. A., Lasota J.-P., Igumenshchev I. V., 2000, *MNRAS*, 314, 775  
Badnell N. R., Bautista M. A., Butler K., Delahaye F., Mendoza C., Palmeri P., Zeppen C. J., Seaton M. J., 2005, *MNRAS*, 360, 458  
Begelman M. C., 1978, *MNRAS*, 184, 53  
Begelman M. C., King A. R., Pringle J. E., 2006, *MNRAS*, 370, 399  
Berghea C. T., Dudik R. P., Weaver K. A., Kallman T. R., 2010, *ApJ*, 708, 364  
Bisikalo D. V., Boyarchuk A. A., Chechetkin V. M., Kuznetsov O. A., Molteni D., 1998, *MNRAS*, 300, 39  
Blaes O., Krolik J. H., Hirose S., Shabaltas N., 2011, *ApJ*, 733, 110  
Blandford R. D., Begelman M. C., 1999, *MNRAS*, 303, L1  
Blandford R. D., Begelman M. C., 2004, *MNRAS*, 349, 68  
Blundell K. M., Mioduszewski A. J., Muxlow T. W. B., Podsiadlowski P., Rupen M. P., 2001, *ApJ*, 562, L79  
Blundell K. M., Bowler M. G., Schmidtbreick L., 2008, *ApJ*, 678, L47  
Bobrick A., Davies M. B., Church R. P., 2017, *MNRAS*, 467, 3556  
Chiang E. I., Goldreich P., 1997, *ApJ*, 490, 368  
Draine B. T., 2011, *Physics of the Interstellar and Intergalactic Medium*. Princeton Univ. Press, Princeton, NJ  
Eggleton P. P., 1983, *ApJ*, 268, 368  
Fabrika S., 2004, *Astrophys. Space Phys. Res.*, 12, 1  
Ferguson J. W., Alexander D. R., Allard F., Barman T., Bodnarik J. G., Hauschildt P. H., Heffner-Wong A., Tamanai A., 2005, *ApJ*, 623, 585  
Ferland G. J. et al., 2017, *Rev. Mex. Astron. Astrofis.*, 53, 385  
Filippenko A. V., Romani R. W., Sargent W. L. W., Blandford R. D., 1988, *AJ*, 96, 242  
Frank J., King A., Raine D. J., 2002, *Accretion Power in Astrophysics*, 3rd edn. Cambridge Univ. Press, Cambridge, p. 398  
Fuller J., 2017, *MNRAS*, 470, 1642  
Ge H., Hjellming M. S., Webbink R. F., Chen X., Han Z., 2010, *ApJ*, 717, 724  
Gladstone J. C., Copperwheat C., Heinke C. O., Roberts T. P., Cartwright T. F., Levan A. J., Goad M. R., 2013, *ApJS*, 206, 14  
Goad M. R., Roberts T. P., Reeves J. N., Uttley P., 2006, *MNRAS*, 365, 191  
Heida M. et al., 2014, *MNRAS*, 442, 1054  
Hirose M., Osaki Y., 1990, *PASJ*, 42, 135  
Hjellming M. S., Webbink R. F., 1987, *ApJ*, 318, 794  
Hubová D., Pejcha O., 2019, *MNRAS*, 489, 891  
Iglesias C. A., Rogers F. J., 1996, *ApJ*, 464, 943  
Igumenshchev I. V., Narayan R., Abramowicz M. A., 2003, *ApJ*, 592, 1042  
Ivanova N., Belczynski K., Kalogera V., Rasio F. A., Taam R. E., 2003, *ApJ*, 592, 475  
Ivanova N. et al., 2013, *A&A Rev.*, 21, 59  
Jiang Y.-F., Stone J. M., Davis S. W., 2014, *ApJ*, 796, 106  
Jiang Y.-F., Stone J. M., Davis S. W., 2019, *ApJ*, 880, 67  
Kaaret P., Ward M. J., Zezas A., 2004, *MNRAS*, 351, L83  
Kaaret P., Feng H., Roberts T. P., 2017, *ARA&A*, 55, 303  
Kilpatrick C. D. et al., 2021, *MNRAS*, 504, 2073  
King A. R., Begelman M. C., 1999, *ApJ*, 519, L169  
Klencki J., Istrate A. G., Nelemans G., Pols O., 2021, *A&A*, 662, 24  
Langer N., 2012, *ARA&A*, 50, 107  
Lau R. M., Heida M., Kasliwal M. M., Walton D. J., 2017, *ApJ*, 838, L17  
Lau R. M. et al., 2019, *ApJ*, 878, 71  
López K. M., Heida M., Jonker P. G., Torres M. A. P., Roberts T. P., Walton D. J., Moon D. S., Harrison F. A., 2017, *MNRAS*, 469, 671  
MacLeod M., Ostriker E. C., Stone J. M., 2018a, *ApJ*, 863, 5  
MacLeod M., Ostriker E. C., Stone J. M., 2018b, *ApJ*, 868, 136  
Marchant P., Pappas K. M. W., Gallegos-García M., Berry C. P. L., Taam R. E., Kalogera V., Podsiadlowski P., 2021, *A&A*, 650, 22  
Margalit B., Metzger B. D., 2016, *MNRAS*, 461, 1154  
Mcley L., Soker N., 2014, *MNRAS*, 445, 2492  
Metzger B. D., Pejcha O., 2017, *MNRAS*, 471, 3200  
Metzger B. D., Zenati Y., Chomiuk L., Shen K. J., Strader J., 2021, *ApJ*, 923, 100  
Narayan R., Yi I., 1994, *ApJ*, 428, L13  
Narayan R., Yi I., 1995, *ApJ*, 444, 231  
Narayan R., Kato S., Honma F., 1997, *ApJ*, 476, 49

- Narayan R., Igumenshchev I. V., Abramowicz M. A., 2000, *ApJ*, 539, 798
- Narayan R., Sądowski A., Penna R. F., Kulkarni A. K., 2012, *MNRAS*, 426, 3241
- Narayan R., Sądowski A., Soria R., 2017, *MNRAS*, 469, 2997
- Paczynski B., 1971, *ARA&A*, 9, 183
- Paczynski B., 1977, *ApJ*, 216, 822
- Paczynski B., Sienkiewicz R., 1972, *AcA*, 22, 73
- Paragi Z., Vermeulen R. C., Fejes I., Schilizzi R. T., Spencer R. E., Stirling A. M., 1999, *A&A*, 348, 910
- Pavlovskii K., Ivanova N., Belczynski K., Van K. X., 2017, *MNRAS*, 465, 2092
- Paxton B. et al., 2015, *ApJS*, 220, 15
- Paxton B. et al., 2019, *ApJS*, 243, 10
- Pejcha O., Metzger B. D., Tomida K., 2016a, *MNRAS*, 455, 4351
- Pejcha O., Metzger B. D., Tomida K., 2016b, *MNRAS*, 461, 2527
- Piran T., 1977, *MNRAS*, 180, 45
- Plavec M., Kratochvil P., 1964, *Bull. Astron. Inst. Czech.*, 15, 165
- Podsiadlowski P., Joss P. C., Hsu J. J. L., 1992, *ApJ*, 391, 246
- Postnov K. A., Yungelson L. R., 2014, *Living Reviews in Relativity*, 17, 3
- Quataert E., Gruzinov A., 2000, *ApJ*, 539, 809
- Quataert E., Shiode J., 2012, *MNRAS*, 423, L92
- Rybicki G. B., Lightman A. P., 1986, *Radiative Processes in Astrophysics*
- Shakura N. I., Sunyaev R. A., 1973, *A&A*, 500, 33
- Shen R. F., Barniol Duran R., Nakar E., Piran T., 2015, *MNRAS*, 447, L60
- Shklovskii I. S., 1981, *Soviet Ast.*, 25, 315
- Shu F. H., Lubow S. H., Anderson L., 1979, *ApJ*, 229, 223
- Smartt S. J., 2015, *PASA*, 32, e016
- Soberman G. E., Phinney E. S., van den Heuvel E. P. J., 1997, *A&A*, 327, 620
- Stone J. M., Pringle J. E., Begelman M. C., 1999, *MNRAS*, 310, 1002
- Sun N.-C., Maund J. R., Crowther P. A., Hirai R., Kashapov A., Liu J.-F., Liu L.-D., Zapartas E., 2021, *MNRAS*, 510, 3701
- Sytov A. Y., Kaigorodov P. V., Bisikalo D. V., Kuznetsov O. A., Boyarchuk A. A., 2007, *Astron. Rep.*, 51, 836
- Tao L., Feng H., Grisé F., Kaaret P., 2011, *ApJ*, 737, 81
- Tao L., Kaaret P., Feng H., Grisé F., 2012, *ApJ*, 750, 110
- Tauris T. M., Langer N., Podsiadlowski P., 2015, *MNRAS*, 451, 2123
- van den Heuvel E. P. J., 1981, *Vistas Astron.*, 25, 95
- van den Heuvel E. P. J., De Loore C., 1973, *A&A*, 25, 387
- van den Heuvel E. P. J., Portegies Zwart S. F., de Mink S. E., 2017, *MNRAS*, 471, 4256
- Vinokurov A., Fabrika S., Atapin K., 2018, *ApJ*, 854, 176
- Wagner R. M., 1986, *ApJ*, 308, 152
- Waisberg I., Dexter J., Petrucci P.-O., Dubus G., Perraut K., 2019, *A&A*, 623, A47
- Walton D. J. et al., 2015, *ApJ*, 806, 65
- Warner B., 1995, *Camb. Astrophys. Ser.*, 28
- Wu S., Fuller J., 2021, *ApJ*, 906, 3
- Yuan F., Narayan R., 2014, *ARA&A*, 52, 529
- Yuan F., Wu M., Bu D., 2012, *ApJ*, 761, 129

## APPENDIX A: EFFECTS OF OPACITY

In this Appendix, we show the dependence of our results on the Rosseland-mean opacity, which affects the cooling of the disc gas by radiative diffusion in the vertical direction. We consider a H-poor solar-metallicity ( $X = 0$ ,  $Z = 0.02$ ) gas composition, as well as a H-rich low-metallicity ( $X = 0.7$ ,  $Z = 0.001$ ) case. The main differences from our fiducial case ( $X = 0.7$ ,  $Z = 0.02$ ) are that the H-poor case has a lower scattering opacity and the low-metallicity case has a weaker iron opacity bump, and the consequence is that L2 mass-loss occurs at a higher mass-transfer rate (for a fixed binary separation and component masses). The opacity tables  $\kappa(\rho, T)$  for all three cases are shown in Fig. A1. We use the boundary values at the same temperature when  $(\rho, T)$  is beyond the boundaries of the given table. This only occurs for wide binary separation  $a \gtrsim 10^3 R_\odot$  and low mass-transfer rate  $|\dot{M}_1| \lesssim 10^{-5} M_\odot \text{ yr}^{-1}$ , and our main results are unaffected.

Then, we show the results of the L2 mass-loss fraction from the outer disc  $f_{\text{L2}}^{\text{outer}}(|\dot{M}_1|, a)$  as a function of mass-transfer rate and binary separation in Fig. A2 (for H-poor solar metallicity) and in Fig. A3 (for H-rich low metallicity). In each of the figures, we compare the result with that from in our fiducial case of H-rich solar metallicity composition.



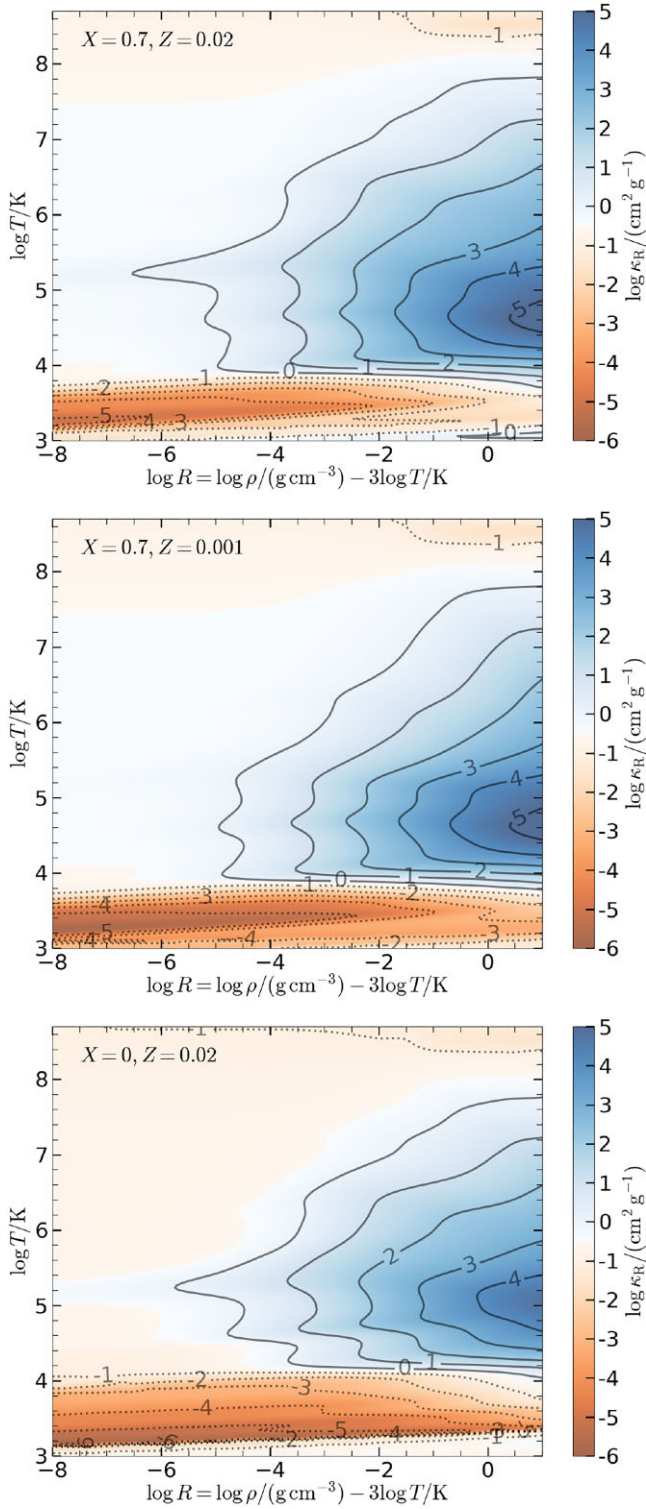


**Figure A1.** Rosseland-mean opacity tables corresponding to three different gas compositions: H-rich solar metallicity ( $X = 0.7, Z = 0.02$ , upper), H-rich low metallicity ( $X = 0.7, Z = 0.001$ , middle), and H-poor solar metallicity ( $X = 0, Z = 0.02$ , bottom panel). Compared to the standard ‘H-rich  $Z_\odot$ ’ case, the low-metallicity case lacks the iron opacity bump near  $T \sim 2 \times 10^5 \text{ K}$ , and the H-poor case has lower electron scattering opacity and lacks the hydrogen opacity bump near  $T \sim 1 \times 10^4 \text{ K}$ .

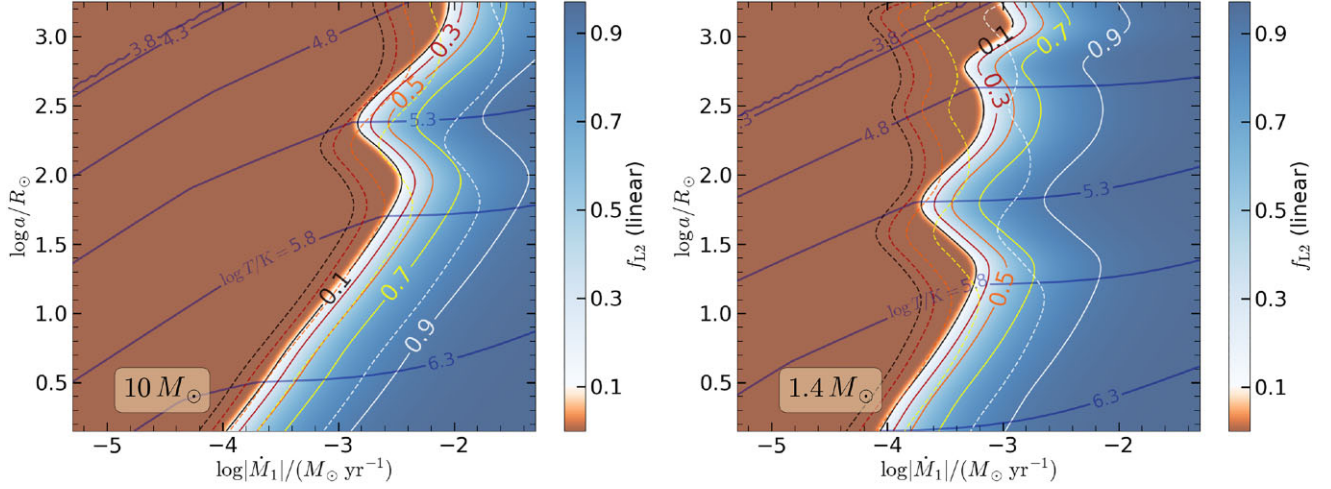


**Figure A2.** The colour-shading and solid contour lines show the L2 mass-loss fraction from the outer disc  $f_{L2}^{\text{outer}}$  (in linear scale) for H-poor solar-metallicity gas composition ( $X = 0$ ,  $Z = 0.02$ ). The left-hand panel is for secondary mass  $M_2 = 10 M_\odot$  (massive star or BH), and the right-hand panel is for  $M_2 = 1.4 M_\odot$  (NS). For both panels, we have fixed the mass ratio  $q = M_2/M_1 = 0.5$  and viscosity parameter  $\alpha = 0.1$ , and we use  $\mu_g = 4/3$  (mean molecular weight for fully ionized helium, see the text below equation 10). Compared to the fiducial case of H-rich solar-metallicity gas (shown by the dashed contours), we find that the main effect of lower hydrogen mass fraction is to reduce the scattering opacity as well as the hydrogen opacity bump near  $T \sim 1 \times 10^4$  K; this increases the Eddington luminosity of the accretor, so higher mass-transfer rates are needed to trigger L2 mass-loss. The effect of the reduced hydrogen opacity bump is only seen on the right-hand panel ( $M_2 = 1.4 M_\odot$ ) for wide binary separations  $a \sim 10^3 R_\odot$ .

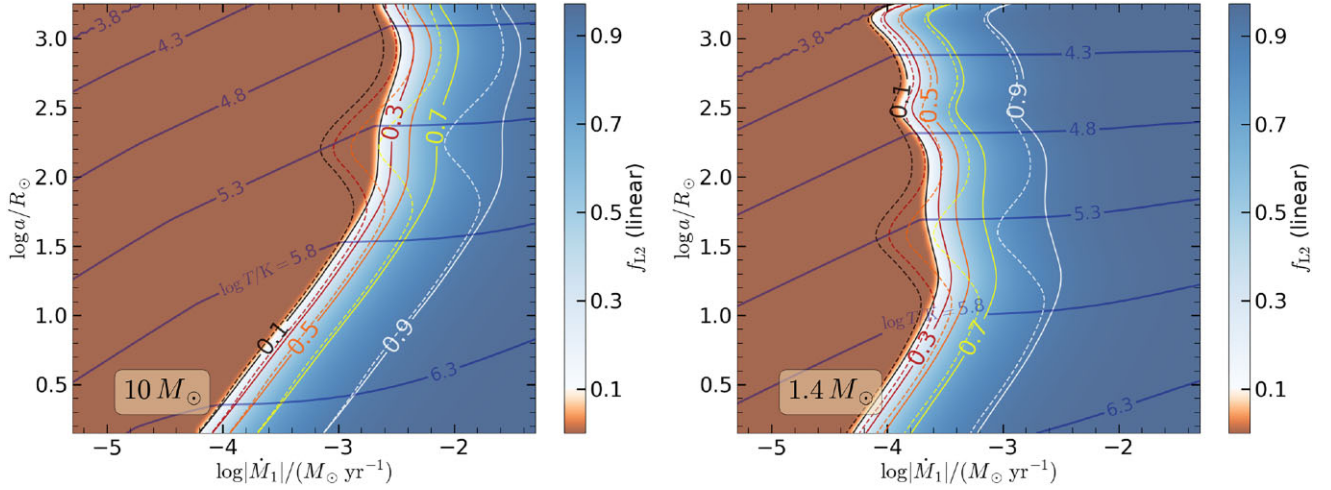


**Figure A3.** The colour-shading and solid contour lines show the L2 mass-loss fraction from the outer disc  $f_{L2}^{\text{outer}}$  (in linear scale) for H-rich low-metallicity gas composition ( $X = 0.7$ ,  $Z = 0.001$ ). The left-hand panel is for secondary mass  $M_2 = 10 M_\odot$  (massive star or BH), and the right-hand panel is for  $M_2 = 1.4 M_\odot$  (NS). For both panels, we have fixed the mass ratio  $q = M_2/M_1 = 0.5$  and viscosity parameter  $\alpha = 0.1$ . Compared to the fiducial case of H-rich solar-metallicity gas (shown by the dashed contours), we find that the main effect of lower metallicity is to reduce the iron opacity bump near  $T \sim 2 \times 10^5$  K; this increases the Eddington luminosity of the accretor, so higher mass-transfer rates are needed to trigger L2 mass-loss.

This paper has been typeset from a  $\text{\LaTeX}$  file prepared by the author.